Cell Reports

Article

BMP-dependent patterning of ectoderm tissue material properties modulates lateral mesendoderm cell migration during early zebrafish gastrulation

Graphical abstract

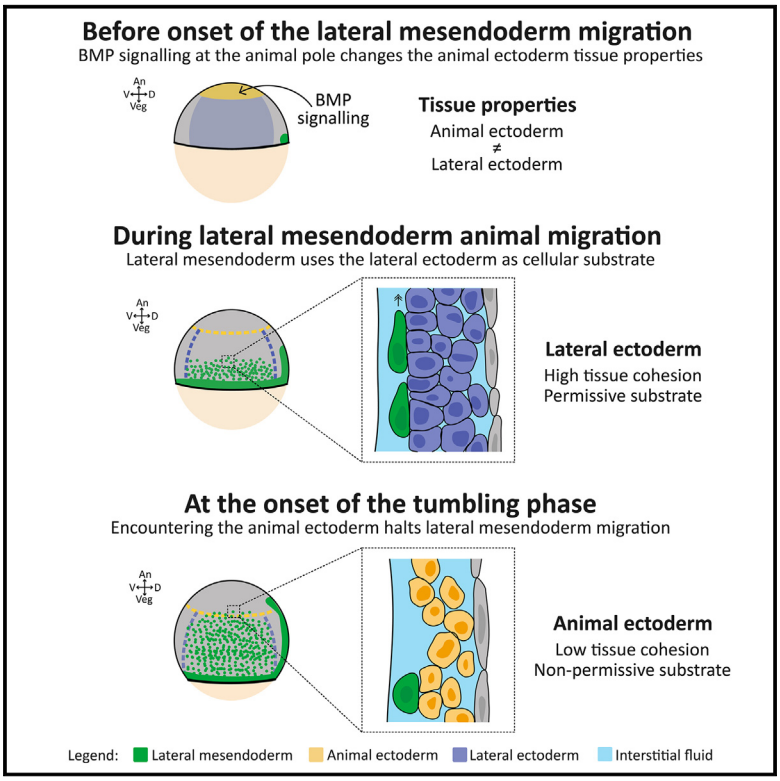

Highlights

- Ectoderm tissue properties are patterned along the animal-vegetal axis
- In the absence of ECM, the lateral mesendoderm (LME) migrates on the ectoderm
- Lateral ectoderm is a permissive substrate, but LME halts when encountering animal ectoderm
- The non-permissiveness of animal ectoderm relies on BMP signaling reducing tissue cohesion

Authors

Stefania Tavano, David B. Brückner, Saren Tasciyan, ..., Alexandra Schauer, Robert Hauschild, Carl-Philipp Heisenberg

Correspondence

tavano.stefania@gmail.com (S.T.), heisenberg@ist.ac.at (C.-P.H.)

In brief

Tavano et al. discovered a novel mechanism controlling lateral mesendoderm (LME) migration during zebrafish gastrulation. LME uses the lateral ectoderm as a permissive substrate for its migration. At the animal pole, LME migration is halted due to bone morphogenetic protein (BMP) signaling modulating ectoderm tissue properties, rendering it non-permissive for LME migration.

Tavano et al., 2025, Cell Reports *44*, 115387
March 25, 2025
https://doi.org/10.1016/j.celrep.2025.115387

CellPress

Cell Reports

CellPress
OPEN ACCESS

Article

BMP-dependent patterning of ectoderm tissue material properties modulates lateral mesendoderm cell migration during early zebrafish gastrulation

Stefania Tavano,[1,2,*] David B. Brückner,[1] Saren Tasciyan,[1] Xin Tong,[1] Roland Kardos,[1] Alexandra Schauer,[1] Robert Hauschild,[1] and Carl-Philipp Heisenberg[1,2,*]

[1]Institute of Science and Technology Austria, Klosterneuburg, Austria

[2]Lead contact

*Correspondence: tavano.stefania@gmail.com (S.T.), heisenberg@ist.ac.at (C.-P.H.)

https://doi.org/10.1016/j.celrep.2025.115387

SUMMARY

Cell migration is a fundamental process during embryonic development. Most studies *in vivo* have focused on the migration of cells using the extracellular matrix (ECM) as their substrate for migration. In contrast, much less is known about how cells migrate on other cells, as found in early embryos when the ECM has not yet formed. Here, we show that lateral mesendoderm (LME) cells in the early zebrafish gastrula use the ectoderm as their substrate for migration. We show that the lateral ectoderm is permissive for the animal-pole-directed migration of LME cells, while the ectoderm at the animal pole halts it. These differences in permissiveness depend on the lateral ectoderm being more cohesive than the animal ectoderm, a property controlled by bone morphogenetic protein (BMP) signaling within the ectoderm. Collectively, these findings identify ectoderm tissue cohesion as one critical factor in regulating LME migration during zebrafish gastrulation.

INTRODUCTION

Cell migration is a fundamental process in organism development and homeostasis, and defects in its regulation are at the basis of various diseases. The extracellular environment plays a pivotal role in the regulation of cell migration. Work *in vitro* and *in vivo* has shown that exposure to pre-existing or self-generated gradients of biochemical signals can guide cells over long distances.[1,2] Moreover, physical confinement can influence the migratory behavior of cells and direct their migration.[3,4] An essential component of the extracellular environment is the extracellular matrix (ECM), on which cells can migrate. In line with this, the biochemical composition and mechanical properties of the ECM have been shown to affect cell migration both *in vivo* and *in vitro*.[5,6] In contrast, much less is known about how cells migrate without the ECM.

A prominent case of ECM-independent cell migration is lateral mesendoderm (LME) migration in the early zebrafish gastrula. In the developing zebrafish embryo, the onset of ECM deposition coincides with the start of gastrulation.[7,8] However, the ECM only forms a distinct and coherent network at late gastrulation.[7,8] Thus, LME migration in the early zebrafish gastrula occurs largely without the ECM. LME migration is characterized by three distinct phases (Figure 1A): upon ingression at the germ ring margin, LME collectively migrates toward the animal pole of the gastrula as a loosely connected population between the yolk cell (YC) membrane and the overlying ectoderm.[9,10] This animal-pole-directed cell migration (animal migration) involves a self-generated gradient of *toddler*[11] (mesoderm) and random walk[10,12] (endoderm), with these two cell-migration modes being coordinated by Cxcl12b/Cxcr4a signaling.[13,14] After a period of persistent motion, the LME animal movement ceases at mid-gastrulation, when LME enters into a second phase characterized by uncoordinated tumbling movements and little displacement.[15,16] This phase is followed by a third phase of convergence movements, where LME undergoes highly persistent and directed migration toward the forming body axis.[9] This third migration phase depends on bone morphogenetic protein (BMP)[17] and non-canonical Wnt signaling[18] and is guided by a gradient of cadherin-mediated cell-cell adhesion,[19] requiring interaction with the ECM.[8]

While past work has provided insight into the molecular and cellular regulation of both animal migration and convergence, comparably little is yet known about why LME ceases moving toward the animal pole at mid-gastrulation and, instead, enters into a tumbling phase. Given that the ECM at mid-gastrulation stage does not yet show any distinct accumulation within the embryo,[7,8] changes in the interaction between LME cells and their surrounding tissues, i.e., the underlying YC and overlying ectoderm germ layer, are likely involved in this process.

RESULTS

Ectoderm is the primary substrate for LME migration

To understand why LME stops migrating toward the animal pole and, instead, turns dorsally, we first analyzed how the LME front migrates during animal migration from early to mid-gastrulation (6.2–8.8 h post fertilization [hpf]) (Figures 1B and S1A; Video

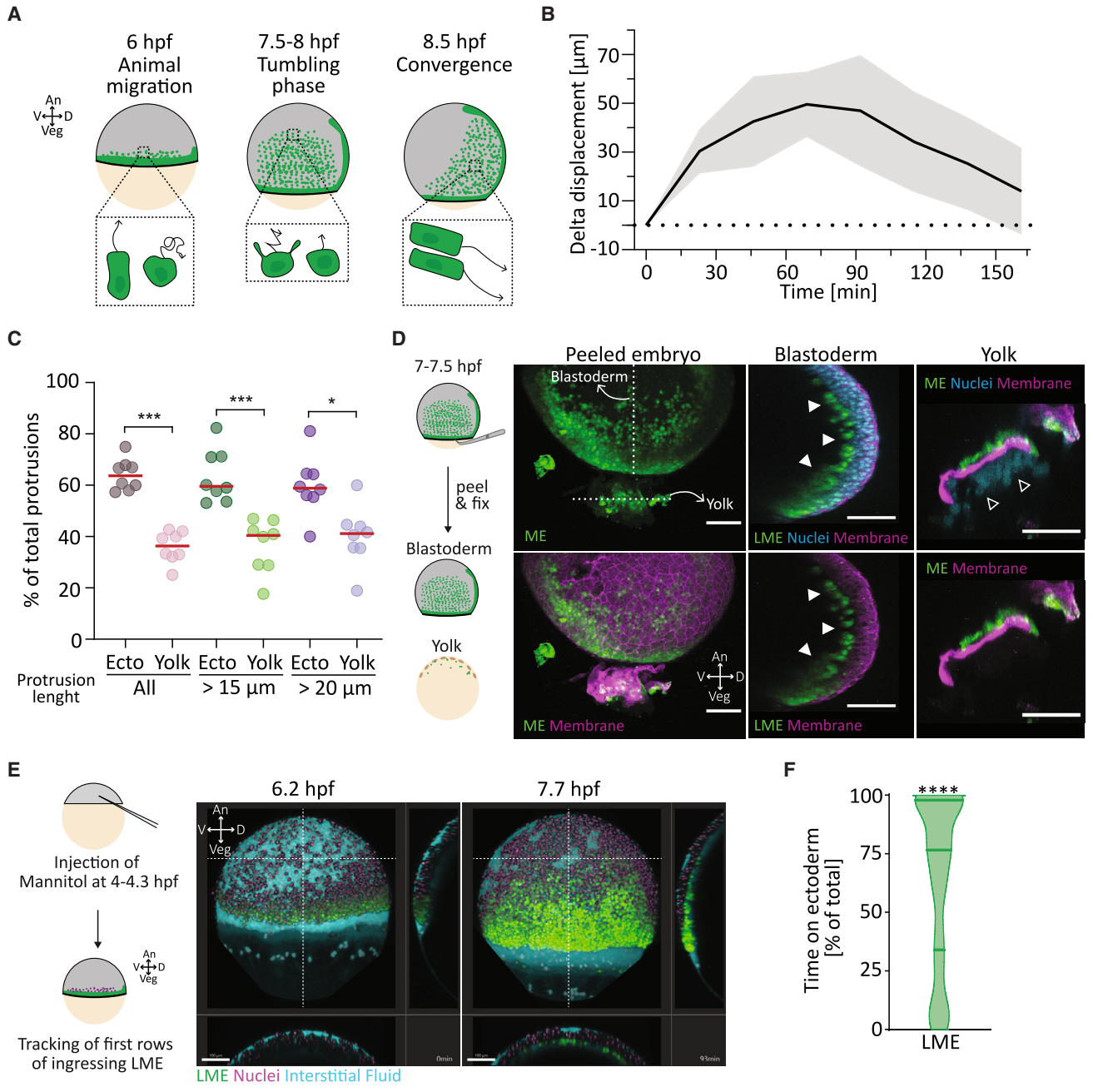

Figure 1. Ectoderm is the primary substrate for lateral mesendoderm animal migration

(A) Schematic representation of lateral mesendoderm (LME) migration during zebrafish gastrulation. An, animal; Veg, vegetal; D, dorsal; V, ventral; hpf, hours post fertilization.

(B) Delta displacement along the animal-vegetal (AnVeg) axis of the LME front over time. Values are shown as mean (solid black line) with standard deviation (SD, light-gray area). Dotted line represents 0 µm on the y axis. Number of embryos, 11. See also Figure S1 and Video S1.

(C) Directionality of LME actin-positive protrusions during animal migration. Scatter dotplot shows the mean percentages of total protrusions of each cell during migration oriented either toward the ectoderm (Ecto) or yolk cell (YC) membrane (Yolk). Red line represents the median. Protrusion length is quantified from the cell center. Number of cells, 8; number of embryos, 2. Total number of protrusions: all, 2,778 (14.1 ± 1.6 SD protrusions per cell per frame [pcpf]); total length from the cell center >15 µm, 1,119 (5.6 ± 1.1 SD pcpf); total length from the cell center >20 µm, 437 (2.2 ± 1.1 SD pcpf). ~2 min 14 s frame rate, t_0 ~6.2 hpf. Statistical test, Mann-Whitney test: ***$p < 0.001$, *$p < 0.05$. See also Video S2.

(D) Yolk-peeling assay. Left: schematic representation of the yolk-peeling assay. Right: maximum-intensity projection of a representative peeled embryo (208 optical sections; z thickness, 2 µm; z step, 1.5 µm). White dashed lines indicate the position of the cross-sections of blastoderm (middle) and yolk (right). Each cross-section is a maximum-intensity projection of 12 optical sections (z thickness, 2 µm; z step, 1.5 µm). Filled arrowheads point at the LME adhering to the

(legend continued on next page)

S1) in *tg*(*sebox*::*eGFP*) embryos, a fish line expressing cytosolic GFP under the control of a pan-mesendodermal marker gene promoter.[20] Consistent with previous observations,[11,15,16] we found that the LME front first moves animally (Figure S1A, 0–92 min), as evidenced by an initial constant increase of its displacement (Figure 1B, 0–69 min) and then transits into a tumbling phase at mid-gastrulation, recognizable by the formation of protrusions in a non-polarized manner (Figure S1A and Video S1, 115–161 min) and a sharp decrease in displacement (Figure 1B, 115–161 min). This confirms the observation that the ability of LME to move animally strongly decreases mid-gastrulation.[15] To further understand the LME migratory behavior before the tumbling phase (6.2–7.7 hpf), we analyzed its migration at the single-cell level. Interestingly, we found that the first LME cells reaching the animal part of the embryo at 7.7 hpf ("most animal," Figure S1B) display migratory properties inherently different from cells following behind (more vegetally) (Figure S1B), as evidenced by a higher persistence and animalward directionality of their migration and, consequently, overall higher displacement along the animal-vegetal (AnVeg) axis (Figures S1C–S1F, LME). To determine whether different progenitor cell types within the LME, i.e., mesoderm and endoderm cells, share this migratory behavior, we analyzed the migration of the endoderm subpopulation within the LME using *tg*(*sox17*::*eGFP*) embryos, a fish line expressing cytosolic GFP under the control of an endoderm marker gene promoter.[21] We found that, similar to all LME cells, the first lateral endoderm cells reaching the animal part of the embryo display a more persistent and directed migration than the cells following behind (Figures S1B–S1F, Endo), suggesting that both mesoderm and endoderm undergo persistent and animally directed migration.

Previous studies have shown that differences in substrate properties, such as stiffness, can affect cell migration.[1–3,5,6,22] To determine whether changes in substrate properties along the AnVeg axis might be responsible for the abrupt slowing down of LME animal migration, we first investigated which substrate LME uses for its migration. In zebrafish, the ECM forms a coherent network between the forming germ layers only at the end of gastrulation.[7,8] Consistently, immunohistochemistry using antibodies against the ECM component fibronectin and phosphorylated focal adhesion kinase (FAK), an essential intracellular signaling mediator of integrin/ECM-mediated cell adhesion,[23] showed only very little fibronectin accumulation at the interface between LME and ectoderm and FAK activity in LME cells during early gastrulation (Figures S1G and S1H). Without the ECM, LME cells can only choose between two possible substrates: the overlaying ectoderm and the underlying YC (Figure S1I). To assess which of these possible substrates they used, we first analyzed the preferred orientation of protrusions of LME cells during their animal migration, focusing on clearly recognizable actin-rich protrusions (Video S2). Interestingly, most protrusions were preferentially oriented toward the ectoderm, suggesting that LME cells are in contact with the ectoderm rather than the YC (Figure 1C). To challenge these findings, we sought to probe whether LME cells preferentially adhere to the ectoderm or the YC by mechanically separating the YC membrane from the blastoderm at 65%–70% epiboly, followed by immediate fixation of both (Figure 1D). After separation, we observed that LME cells were found mainly on the ectoderm rather than the YC membrane, suggesting that they preferentially adhere to the ectoderm. To further challenge this suggestion, we tested which substrate LME cells prefer if unable to touch both substrates simultaneously. To this end, we injected 350 mM mannitol (an inert sugar) between blastoderm cells at the sphere-to-dome stage (4–4.3 hpf), which we previously showed to increase interstitial fluid accumulation at the YC-to-ectoderm boundary.[24] LME cells migrating into this enlarged fluid-filled space had to choose between the ectoderm and YC as their migration substrate (Figure 1E and Video S3). In mannitol-injected embryos, LME cells displayed animal migration indistinguishable from uninjected control embryos (Figures S2A–S2D, LME). When analyzing whether LME cells use the YC or the ectoderm for their animal migration, we found that they preferred the ectoderm (Figure 1F, median 76.1), suggesting that the latter is their primary substrate. Lateral endoderm cells, in contrast, could be subdivided into two roughly equal subpopulations (Figure S2E, median 54.3), one predominantly using the ectoderm and the other the YC membrane as their substrate for migration (Video S4). Moreover, we found that lateral endoderm migration persistence and displacement along the AnVeg axis, but not their overall directionality, were reduced in mannitol-injected embryos (Figures S2A–S2D, Endo), indicating that lateral endoderm cells require close spatial proximity with both ectoderm and YC for proper migration.

Finally, we asked whether and how migrating on the ectoderm affects LME and lateral endoderm animal migration. We found a positive correlation between displacement along the AnVeg axis and time spent migrating on the ectoderm for LME and lateral endodermal cells (Figure 2A). To further challenge these findings, we separately analyzed cells predominantly migrating on the ectoderm or the YC (Figures 2B, S2F, and S2G). Notably, we observed that LME and lateral endoderm had the highest displacement and persistence when migrating on the ectoderm (Figures 2C, 2D, S2H, and S2I). Moreover, cells using mainly the ectoderm showed a higher animal directionality and displacement along the AnVeg axis than cells using the YC as their migrational substrate (Figures 2E, 2F, S2J, and S2K). Collectively, this

blastoderm in absence of the YC membrane. Empty arrowheads point at the yolk syncytial layer (YSL) nuclei. Green, eGFP (mesendoderm, ME or LME); magenta, mCherry (membrane); cyan, DAPI (nuclei). Scale bar, 100 μm

(E) Mannitol-induced detachment of the blastoderm from the yolk. Left: schematic representation of the experimental setup. Right: still images of LME cells (lateral view) from a representative time-lapse video at the start (left, 6.2 hpf) and end (right, 7.7 hpf) of the migration period. White dashed lines indicate the position of the yz (right) and xz (bottom) cross-sections. Green, eGFP (LME cells); magenta, H2A-mCherry (nuclei); cyan, Alexa Fluor 647 dextran (interstitial fluid). ~2 min frame rate. Scale bar, 100 μm. See also Video S3.

(F) Time the LME cells use the ectoderm as substrate for migration. Data are shown as percentage of the total time of migration. Number of cells, 163; number of embryos, 3. Statistical test, one-sample Wilcoxon test: ****$p < 0.0001$. See also Figure S2.

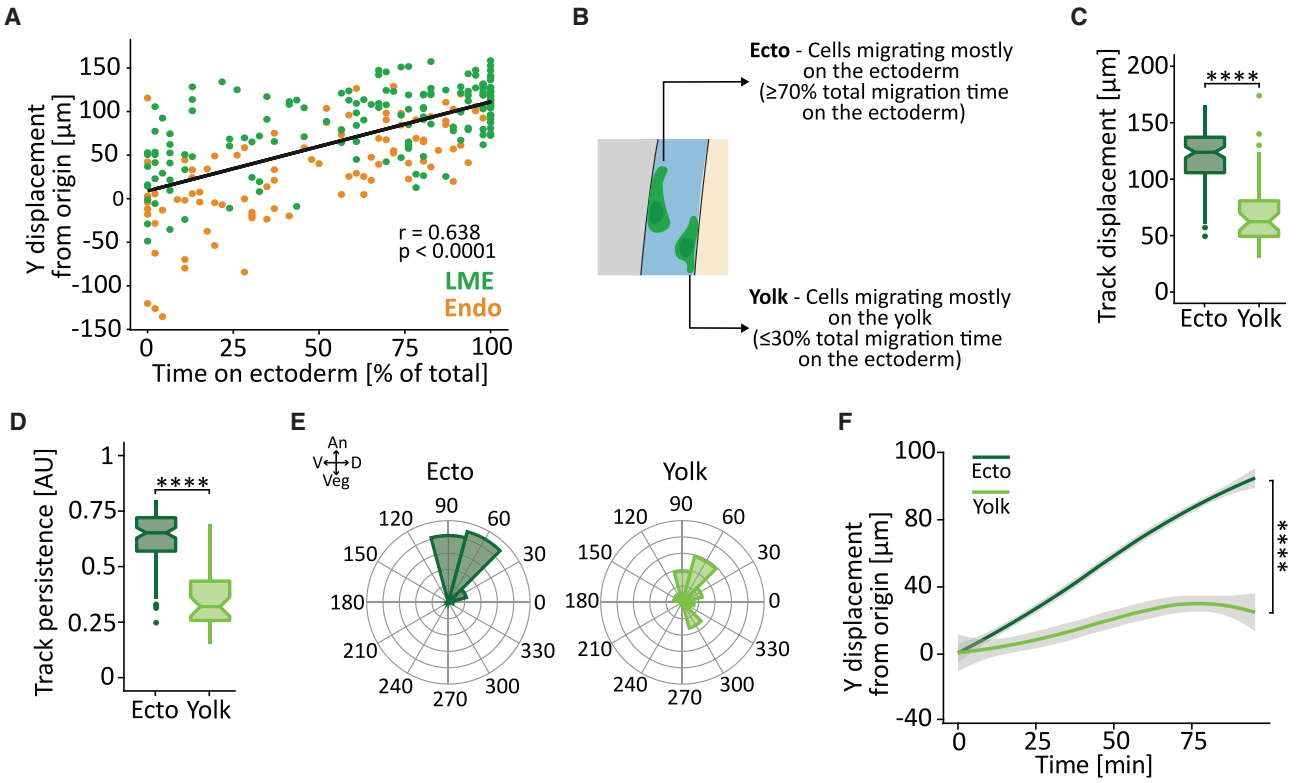

Figure 2. Lateral mesendoderm cells migrating on the ectoderm display most-pronounced animal migration

(A) Correlation between the time lateral mesendoderm (LME) and endoderm (Endo) cells migrate on the ectoderm (x axis) and their displacement along the animal-vegetal (AnVeg) axis, expressed as final y-displacement from the origin (y axis). Green dots, LME; orange dots, Endo cells. Statistical test, Spearman *r*. Number of pairs, 259 (163 LME cells from 3 embryos; 96 Endo cells from 2 embryos). See also Figure S2.

(B) Explanation of the subgrouping used for the analyses in (C)–(F) and in Figure S2. Cells using ectoderm as substrate for either more than 70% or less than 30% of their migration time (see also graphs in Figures S2F and S2G) were defined in the analysis as cells migrating mostly on the ectoderm (Ecto) or mostly on the yolk cell (YC) membrane (Yolk), respectively.

(C) Total displacement of LME cells using mostly the ectoderm (Ecto, dark green) or the YC membrane (Yolk, light green) as substrate for their migration. Number of cells: Ecto, 99; yolk, 42. Number of embryos, 3. Statistical test, Mann-Whitney test: ****$p < 0.0001$.

(D) Migration persistence of LME using mostly the ectoderm (Ecto, dark green) or the YC membrane (Yolk, light green) as substrate for their migration. Number of cells: Ecto, 99; yolk, 42. Number of embryos, 3. Statistical test, Mann-Whitney test: ****$p < 0.0001$.

(E) Migration directionality of LME cells using mostly the ectoderm (Ecto, dark green) or the YC membrane (Yolk, light green). An, animal; Veg, vegetal; D, dorsal; V, ventral. Number of cells: Ecto, 99; yolk, 42. Number of embryos, 3.

(F) Displacement (y displacement) of LME cells along the AnVeg axis over time. Solid line represents the mean; gray ribbon displays confidence interval. LME mostly using the ectoderm (Ecto) or the YC membrane (Yolk) as substrate for their migration are shown in dark green and light green, respectively. Number of cells: Ecto, 99; yolk, 42. Number of embryos, 3. Statistical test on the final y displacement, Mann-Whitney test: ****$p < 0.0001$.

suggests that LME preferentially uses the ectoderm as its substrate for migration and that migrating on the ectoderm promotes LME and lateral endoderm animal migration.

Ectoderm patterning along the AnVeg axis modulates LME animal migration

Given the critical role of the ectoderm in promoting LME animal migration, we asked whether local differences in ectoderm properties along the AnVeg axis might be responsible for the sharp slowing down of LME migration at mid-gastrulation. To address this possibility, we performed ectoderm tissue transplantation experiments in which we displaced the endogenous lateral ectoderm tissue from host embryos at germ ring (5.7 hpf) by adding either animal (AtL Ecto, heterotypic transplantation) or lateral (LtL Ecto, homotypic transplantation) ectoderm from donor embryos at the same developmental stage (Figures 3A and 3B; Video S5). As expected, homotypic LtL Ecto transplantation did not affect LME migratory behavior compared to non-transplanted embryos (Figures 3C–3F, S3A, and S3B). In contrast, heterotypic AtL Ecto transplantation substantially decreased LME persistence and displacement along the AnVeg axis, resulting in a significant reduction in the ability of LME cells to reach the animal part of the gastrula before entering into the tumbling phase (Figures 3C–3F, S3A, and S3B). Conversely, displacing animal ectoderm by lateral ectoderm extended the range of LME animal migration (Figures 3G and 3H), further supporting the notion that animal ectoderm is a less-permissive substrate for LME animal migration than lateral ectoderm.

CellPress
OPEN ACCESS

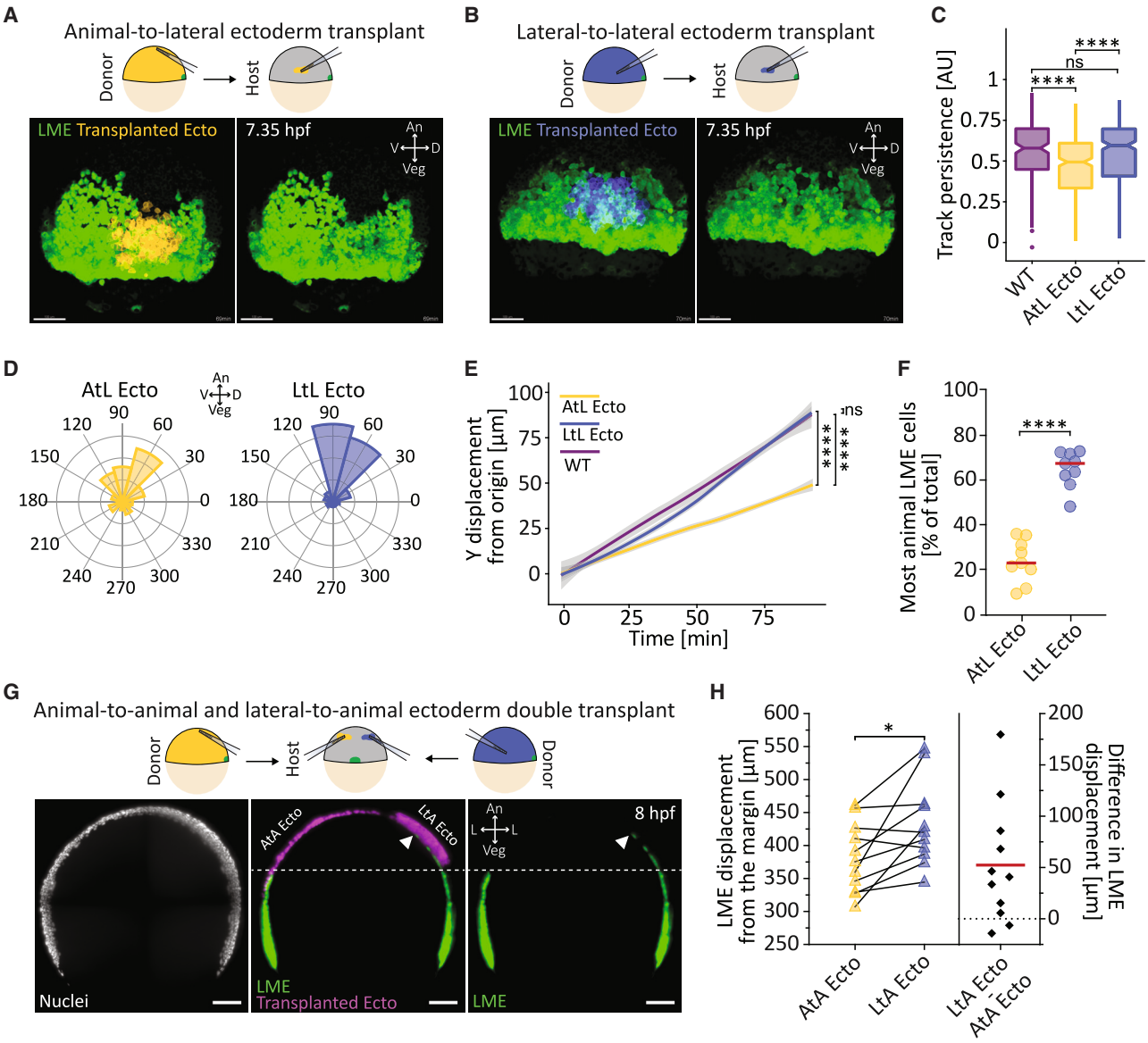

Figure 3. Ectoderm modulates lateral mesendoderm animal migration

(A and B) Animal-to-lateral (AtL heterotypic) (A) and lateral-to-lateral (LtL homotypic) (B) ectoderm transplantation assay. Upper: schematic representation of the experimental setup. Lower: fluorescence images of lateral mesendoderm (LME) cells and transplanted animal (AtL Ecto, yellow, A) or lateral (LtL Ecto, blue, B) ectoderm (lateral view) from representative time lapses ~70 min after the start of LME migration (~7.35 hpf). Green, eGFP (LME cells); yellow, membrane RFP (AtL Ecto); blue, membrane RFP (LtL Ecto). Scale bar, 100 µm. An, animal; Veg, vegetal; D, dorsal; V, ventral. See also Video S5.

(C) Migration persistence of LME cells in transplanted versus non-transplanted wild-type (WT) embryos. Number of cells: 173 from 3 WT (purple), 327 from 9 AtL Ecto (yellow), 327 form 9 LtL Ecto (blue). Statistical test, Mann-Whitney test: ns, not significant; ****$p < 0.0001$. See also Figure S3.

(D) Migration directionality of LME cells in transplanted embryos. Number of cells, 327 from 9 AtL Ecto (yellow); 327 from 9 LtL Ecto (blue). See also Figure S3. Dataset for WT in (C) and (D) corresponds to data shown in Figure S1.

(E) Displacement (y displacement) of LME cells along the animal-vegetal (AnVeg) axis over time in transplanted versus WT embryos. Solid line represents the mean; gray ribbon displays confidence interval. Number of cells, 173 from 3 WT (purple), 327 from 9 AtL Ecto (yellow), 327 from 9 LtL Ecto (blue). Statistical test on the final y displacement, Mann-Whitney test: ns, not significant; ****$p < 0.0001$. See also Figure S3.

(F) Percentage of most animally migrating LME cells (for definition see also Figure S3) in transplanted embryos. Red line represents the median. Number of embryos, 9 AtL Ecto (yellow) and 9 LtL Ecto (blue). Statistical test, Mann-Whitney test: ****$p < 0.0001$.

(G) Animal-to-animal (homotypic, AtA Ecto) and lateral-to-animal (heterotypic, LtA Ecto) ectoderm double-transplantation assay. Upper: schematic representation of the experimental setup. Lower: maximum-intensity projection of ten lateral-to-lateral optical sections (z thickness: 4 µm; z step: 2 µm) showing the fluorescent signal of LME cells (green) in a double-transplanted embryo. AtA Ecto on the left, LtA Ecto on the right. Green, eGFP (LME cells); magenta, membrane RFP/H2B-mCherry (transplanted ectoderm from donor embryos); gray, DAPI (nuclei). Dashed line, extent of LME migration on the AtA Ecto side; full white arrowhead, extent of LME migration on the LtL Ecto side. L, lateral. Scale bar, 100 µm.

(legend continued on next page)

Since substrate material properties are thought to play a pivotal role in modulating cell migration,[1,3,25] we asked whether animal and lateral ectoderm might show different tissue material properties during gastrulation. In the transplantation experiments where lateral ectoderm was transplanted into the animal pole (Figure 3G), we noted that these transplants remained thicker during the course of epiboly compared to control transplants where animal ectoderm was transplanted into the animal pole. This points to the possibility that lateral and animal ectoderm might thin at different rates. To test this possibility, we systematically analyzed how ectoderm thickness changes when spreading over the YC during LME animal migration (6.2–7.7 hpf, Figures 4A–4C). Interestingly, we found that the epibolizing ectoderm thins faster at the animal pole than near its margin (Figures 4B and 4C; Video S6). To relate these findings to LME migration, we subdivided the ectoderm into "lateral" ectoderm, being in contact with migrating LME, and "animal" ectoderm, being devoid of migrating LME, and quantified their changes in tissue thickness during the period of LME animal migration. At the end of LME animal migration (7.7 hpf), the lateral ectoderm showed a decrease in thickness of 27.5% (0.735 ± 0.122 SD), while the animal ectoderm reduced its thickness by 62.7% (0.373 ± 0.075 SD) (Figures 4A–4D). Together, these data indicate that, similar to the blastoderm at doming,[26] epibolizing ectoderm undergoes differential thinning.

During epiboly, the thinning of the ectoderm occurs as an effect of the forces emanating from the underlying yolk syncytial layer (YSL), pulling the blastoderm margin toward the vegetal pole of the gastrula.[27] Those pulling forces are, therefore, expected to be larger near their origin (the margin) than away from it (the animal pole). Thus, the more pronounced tissue thinning at the animal pole is likely due to differential ectoderm material properties rather than pulling forces along its AnVeg axis. To further conceptualize these findings, we developed a minimal ectoderm thinning model for investigating whether this differential ectoderm thinning could result from spatial differences in tissue viscosity[26] (Figures 4E and S3C–S3H). We assumed that the ectoderm is a passive fluid with a conserved volume and that with epiboly progressing the ectodermal tissue is subjected to an external pulling force, causing its elongation with a constant speed of approximately 1.5 μm/min, corresponding to the speed by which the blastoderm spreads over the YC.[27] We first assumed equal viscosity throughout the ectoderm and asked how the tissue thickness changes over time. We found that the tissue thickness decreases equally in animal and lateral regions of the ectoderm (Figures S3C–S3E). Next, we imposed a pattern of viscosity, with viscosity being highest near the margin and lowest at the animal pole (Figures 4E and S3F). Interestingly, we found that the animal ectoderm undergoes faster thinning compared to the lateral ectoderm (Figures 4G, S3G, and S3H) and that this thinning behavior matched the ectoderm tissue-spreading behavior observed experimentally during LME migration (Figures 4D and 4F). Together, these data indicate that differences in ectoderm tissue viscosity along its AnVeg axis can explain its differential thinning behavior.

We have previously shown that in the early zebrafish embryo, the cellular organization of the blastoderm at the onset of doming (4.3 hpf) differs between its center and margin, with the margin forming a more cohesive tissue than the center.[26] We further showed that these differences in cell connectivity lead to the blastoderm center being less viscous than the margin.[28] We thus hypothesized that similar variations in tissue cohesiveness might be responsible for the observed differences in ectoderm thinning and viscosity along its AnVeg axis. To challenge this hypothesis, we quantified the animal and lateral ectoderm cell fraction, the fraction of cells in a tissue volume consisting of cells and interstitial fluid, previously shown to be directly related to cell connectivity and tissue rigidity.[28] Remarkably, we observed that the lateral ectoderm had a higher cell fraction (97% on average) than the animal ectoderm (87% on average) during the period of LME animal migration (Figures 5A, 5B, S4A, and S4B; Video S7), suggesting that animal ectoderm is less compact than the lateral ectoderm. To determine whether the smaller cell fraction at the animal pole is due to fewer cell-cell contacts, we analyzed the percentage of cell perimeter occupied by cell-cell contacts in the animal and lateral ectoderm. In the animal ectoderm, the percentage of cell perimeter in contact with other ectoderm cells was considerably smaller than in the lateral ectoderm (Figures S4C and S4D; Video S8), suggesting that the animal ectoderm is less cohesive than lateral ectoderm. We have previously shown that cell-cell contact size is determined by the ratio of cortical tensions at the cell-cell to the cell-outside medium interfaces.[27–30] Thus, we hypothesized that the higher cell fraction and cell-cell contact engagement in the lateral compared to animal ectoderm is due to a lower ratio of these interfacial tensions. To test this, we quantified the contact angle between cells as a readout of the ratio of cortical tensions at the cell-cell to the cell-medium interfaces,[27–30] within the lateral and animal ectoderm when LME animal migration was under way (28 min from the onset of animal migration) (Figures 5C and 5D). In agreement with our results on cell fraction and cell-cell contact engagement, we found that the contact angle was significantly higher and, thus, the ratio of cortical tensions at the cell-cell to the cell-medium interfaces lower, in the lateral compared to the animal ectoderm (Figure 5E, on average 0.78 in the lateral ectoderm, 0.87 in the animal ectoderm). Collectively, these findings suggest that animal ectoderm shows a lower cohesiveness than lateral ectoderm and that this difference in tissue cohesion is responsible for the observed difference in ectodermal thinning.

To establish a causative link between ectoderm tissue properties and LME animal migration, we first investigated whether the animal and lateral ectoderm tissues kept their characteristic differences in tissue cohesion after being transplanted into the host embryos. Quantifying the cell fraction in LtL Ecto and AtL Ecto

(H) Difference in LME displacement along the AnVeg axis at 8 hpf in double-transplanted embryos. Left: displacement of the LME front (left y axis). Values are shown as median (triangles). Contralateral sides of the same embryos are connected by a black line. Yellow, AtA Ecto; blue, LtA Ecto. Right: difference in LME displacement from the margin (right y axis). Diamonds represent the difference of LME displacement between the AtA Ecto and LtA Ecto sides for each embryo. Red line represents the median. Number of embryos, 11. Statistical test, Paired t test: $*p < 0.05$.
In (C) and (E), datasets for WT embryos correspond to data shown in Figure S2.

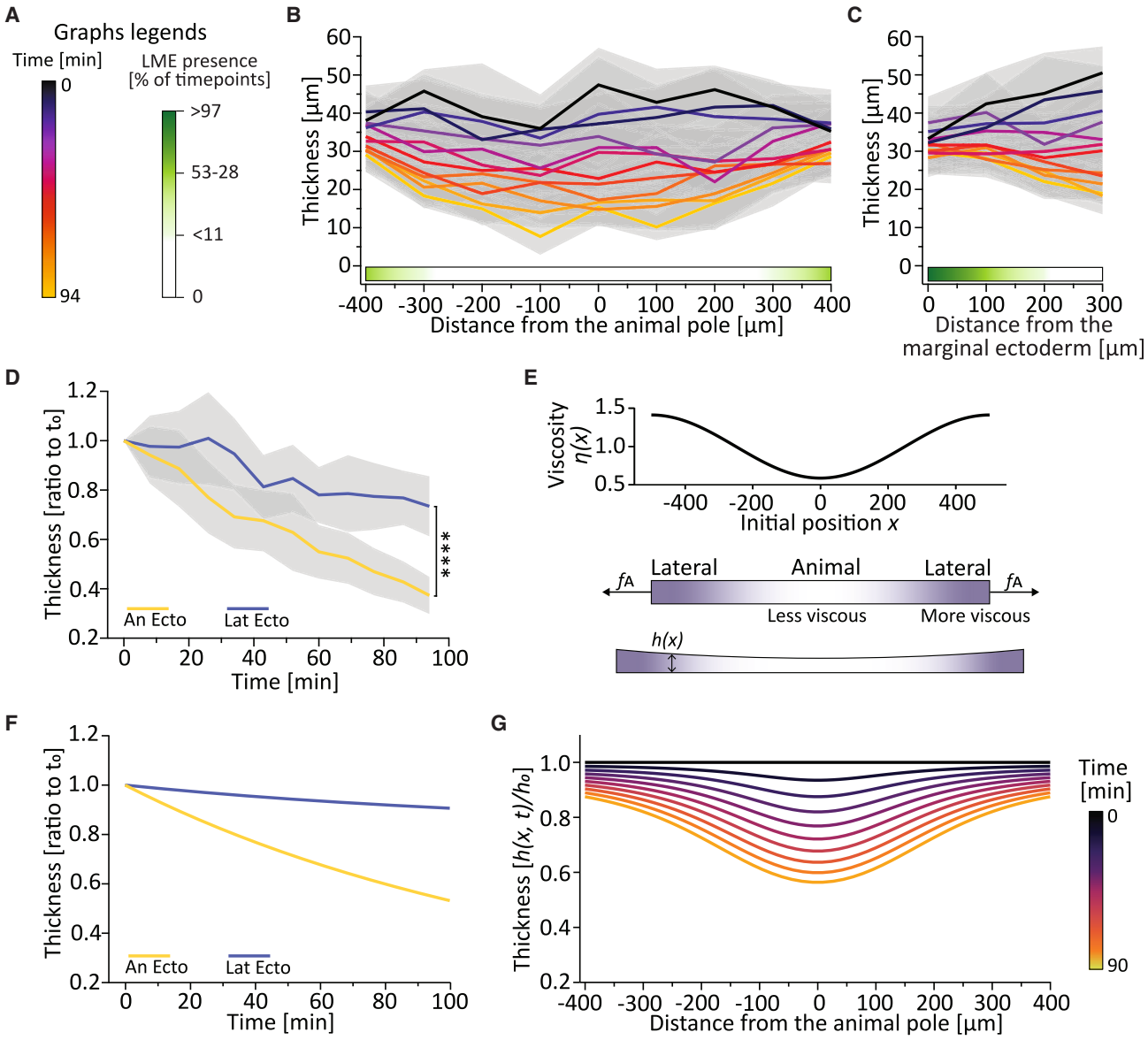

Figure 4. Lateral ectoderm and animal ectoderm undergo differential thinning

(A–D) Ectoderm thickness as a function of developmental time at the animal pole (B) or the lateral side (C) of the gastrula. In (A), developmental time in minutes (min) is shown as a fire colormap, and relative position of the LME along the animal-to-vegetal extent of the ectoderm is shown as a green gradient representing the percentage of total time points. In (B) and (C), ectoderm thickness is shown at the animal pole and in 100-µm-wide bins lateral to the animal pole (x axis) (B) and in the most marginal ectoderm (100–150 µm from the embryo equator) and 100-µm-wide bins animal to the margin (x axis) (C). Values are shown as mean (solid line) with SD (light-gray area). Green gradient bar represents the presence of LME in a specific position (see also A). Number of embryos: animal pole view (B), 6; lateral view (C), 6. In (D), for each embryo, bins were defined as either lateral ectoderm (Lat Ecto, blue), in cases when the ectoderm was in contact with the LME at least for one time point during the imaging period, or animal ectoderm (An Ecto, yellow), in cases when the ectoderm was not in contact with LME during the entire imaging period. Thickness is shown as ratio to the thickness at the onset of LME migration (t_0). Values are shown as mean (solid line) with SD (light-gray area). Number of embryos, 12. Statistical test, two-way ANOVA: ****$p < 0.0001$. See also Video S6.

(E–G) Model of the ectoderm thickness as a function of developmental time. Ectoderm tissue is modeled as a passive fluid with patterned viscosity from the animal pole (lowest) to the margin (highest) and subjected to an external constant pulling force (f_A), which causes an increase of tissue length with a speed of ~1.5 µm/min (corresponding to the experimentally measured blastoderm epiboly speed) (E). In (F), animal (An Ecto, yellow) and lateral (Lat Ecto, blue) ectoderm thickness is shown as ratio to the thickness at t_0. Animal ectoderm corresponds to 200 µm at the animal pole, while lateral ectoderm corresponds to 200 µm at the margin. In (G), ectoderm thickness was quantified as a function of time (90 min, fire colormap) at the animal pole and 400 µm lateral to it (x axis). See also Figure S3.

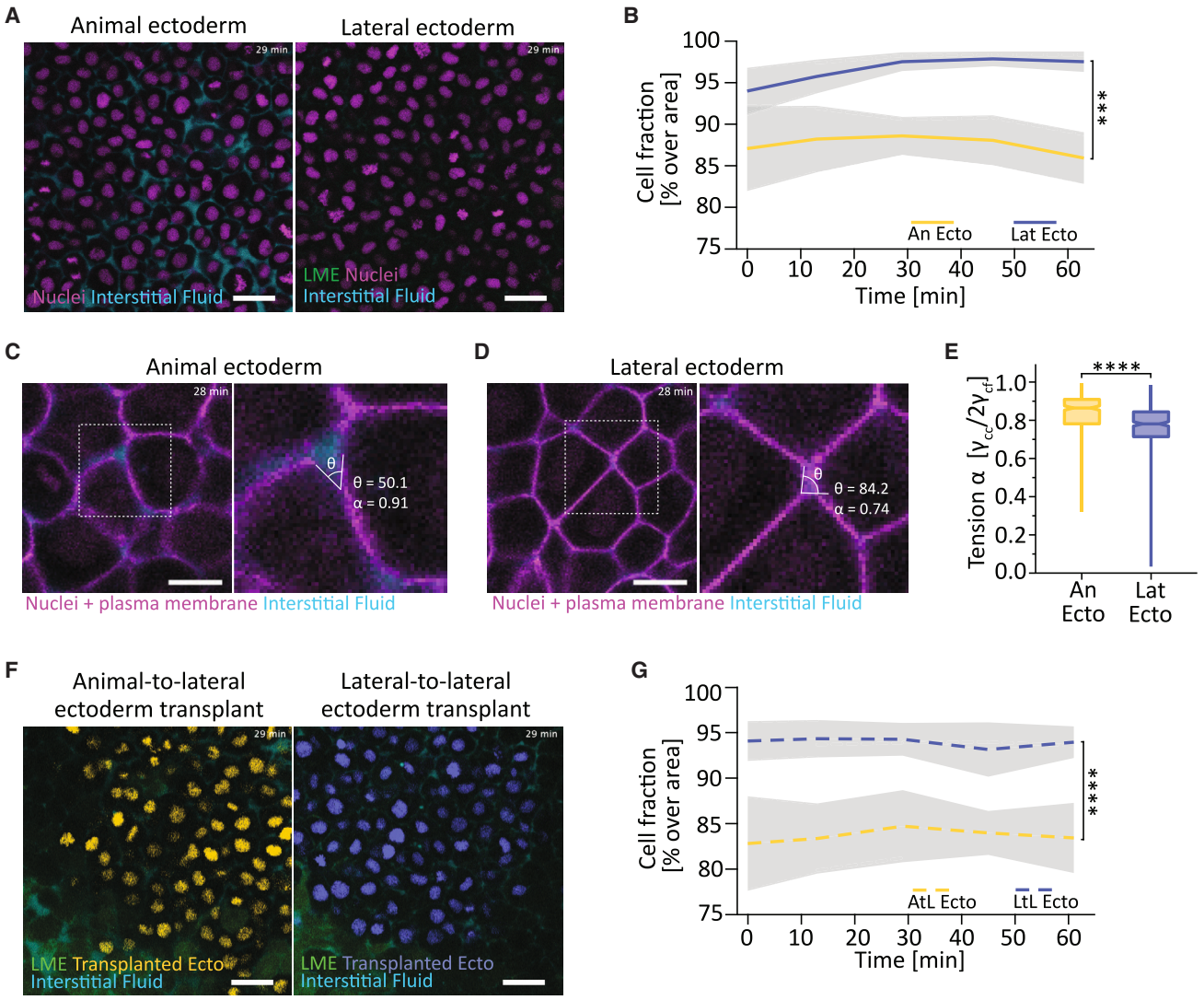

Figure 5. Lateral ectoderm and animal ectoderm display different cell fractions

(A) Fluorescence images of animal (left) and lateral (right) ectoderm. Images are maximum-intensity projection of stacks of three 1-μm optical sections (z-step size, 1.5 μm). Green, eGFP (lateral mesendoderm [LME] cells); magenta, H2A-mCherry (nuclei); cyan, Alexa Fluor 647 dextran (interstitial fluid). Scale bar, 25 μm. See also Figure S4 and Video S9.

(B) Cell fraction in the animal and lateral ectoderm. Values are shown as mean (solid line) with SD (light-gray area). Number of embryos: animal ectoderm (An Ecto, yellow), 5; lateral ectoderm (Lat Ecto, blue), 5. Statistical test, two-way ANOVA: ***$p < 0.001$. See also Figure S4 and Video S7.

(C and D) Fluorescence images of animal (An Ecto, C) and lateral (Lat Ecto, D) ectoderm. Dashed area demarcates the area shown in the respective right panels with exemplary contact angles (θ) used to determine the relative cell tension (α). Images are single 1-μm-thick optical sections. Magenta, H2B-mCherry and membrane RFP (nuclei and cell membrane); cyan, Alexa Fluor 647 dextran (interstitial fluid). Scale bar, 10 μm.

(E) Relative cell tension (α) in the animal and lateral ectoderm 28 min after the onset of LME migration (~6.2 hpf). Number of contact angles: 574 from 3 An Ecto (yellow), 589 from 3 Lat Ecto (blue). Statistical test, Mann-Whitney test: ****$p < 0.0001$.

(F) Fluorescence images of animal-to-lateral (AtL Ecto, yellow, left) and lateral-to-lateral (LtL Ecto, blue, right) ectoderm transplants. Images are maximum-intensity projection of stacks of three 1-μm optical sections (z-step size, 1.5 μm). Green, eGFP (LME cells); yellow, H2A-mCherry (nuclei, AtL Ecto); blue, H2A-mCherry (nuclei, LtL Ecto); cyan, Alexa Fluor 647 dextran (interstitial fluid). Scale bar, 25 μm. See also Figure S4 and Video S9.

(G) Cell fraction in AtL and LtL ectoderm transplants. Values are shown as mean (dashed line) with SD (light-gray area). Number of embryos: 11 AtL Ecto (yellow), 12 LtL Ecto (blue). Statistical test, mixed-effect analysis: ****$p < 0.0001$.

transplants showed that the latter had a smaller cell fraction than the LtL Ecto (Figures 5F, 5G, S4E, and S4F; Video S9), similar to the situation in non-transplanted embryos. To test whether the differences in tissue cohesion between animal and lateral ectoderm transplants are decisive for their influence on LME animal migration, we increased cell contractility in the animal ectoderm by overexpressing constitutively active (CA) Ras homolog family member A (RhoA),[29] previously shown to increase tissue

CellPress
OPEN ACCESS

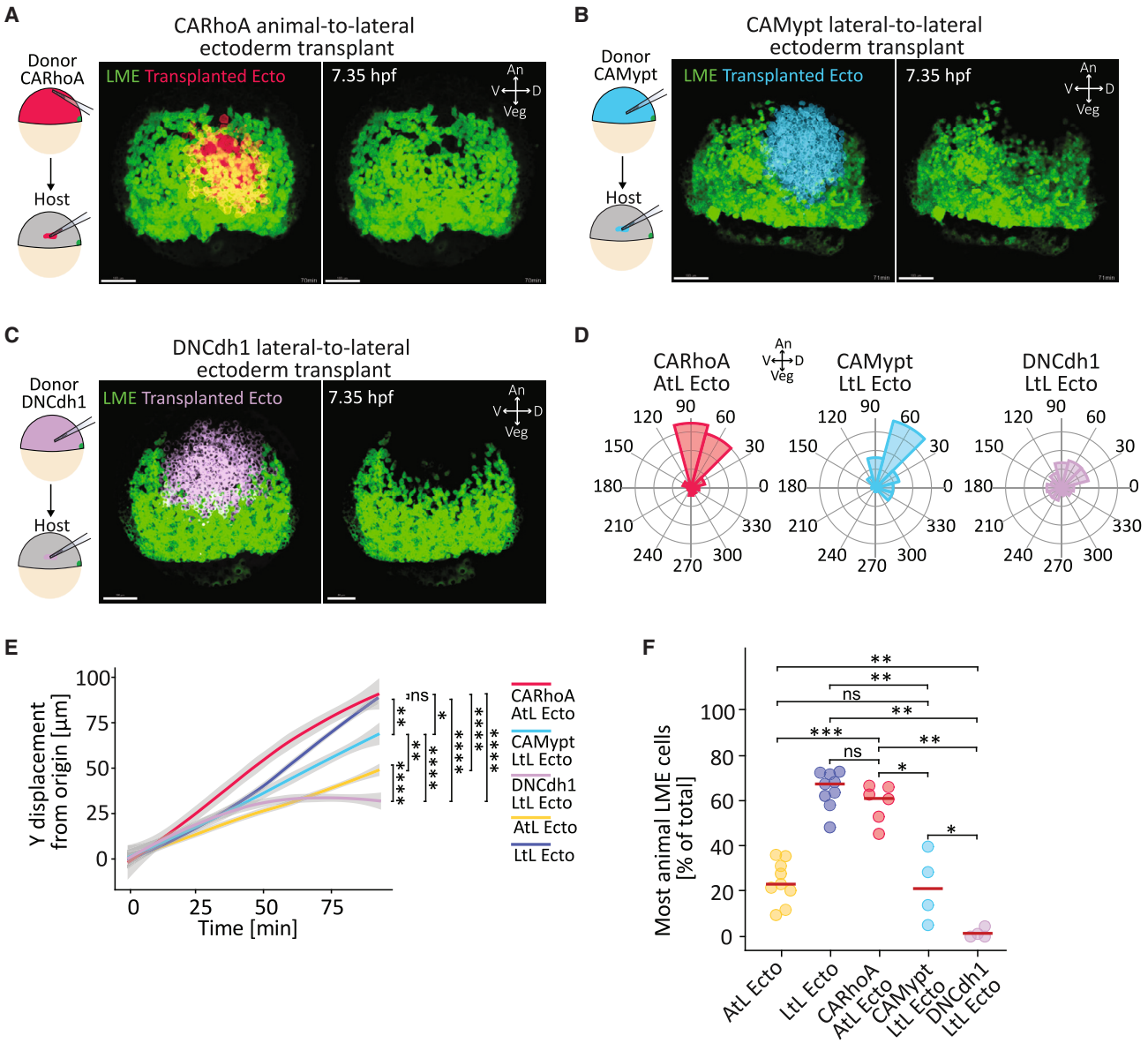

Figure 6. Modulation of cell contractility or cell-cell adhesion in the ectoderm reverses the effect of animal and lateral ectoderm on lateral mesendoderm migration

(A and B) Constitutively active RhoA (CARhoA)-overexpressing animal-to-lateral (AtL) and constitutively active Mypt (CAMypt)-overexpressing lateral-to-lateral (LtL) ectoderm transplant assay. On the left, schematic representation of the experimental setup. On the right, fluorescence images of lateral mesendoderm (LME) cells and transplanted CARhoA-overexpressing animal (CARhoA AtL Ecto, red, A) or CAMypt-overexpressing lateral (CAMypt LtL Ecto, light blue, B) ectoderm (lateral view) from representative time lapses ~70 min after the start of LME migration (~7.35 hpf). Green, eGFP (LME cells); red, membrane RFP (CARhoA AtL Ecto); light blue, membrane RFP (CAMypt LtL Ecto). Scale bar, 100 µm. An, animal; Veg, vegetal; D, dorsal; V, ventral. See also Figure S4 and Video S10.

(C) Dominant negative Cdh1 (DNCdh1)-overexpressing LtL ectoderm transplantation assay. On the left, schematic representation of the experimental setup. On the right, fluorescence images of LME cells and DNCdh1-overexpressing lateral (DNCdh1 LtL Ecto, lilac) ectoderm (lateral view) from representative time-lapse movies ~70 min after the start of LME migration (~7.35 hpf). Green, eGFP (LME cells); lilac, 10,000 MW Alexa Fluor 647 dextran (DNCdh1 LtL Ecto). Scale bar, 100 µm. See also Figure S4 and Video S10.

(D) Migration directionality of LME cells in CARhoA AtL Ecto (red), CAMypt LtL Ecto (light blue), and DNCdh1 LtL Ecto (lilac) transplanted embryos. Number of cells: 292 from 6 CARhoA AtL Ecto (red), 162 from 4 CAMypt LtL Ecto (light blue), 325 from 4 DNCdh1 LtL Ecto (lilac).

(E) Displacement (y displacement) along the animal-vegetal (AnVeg) axis of LME cells over time in transplanted embryos. Solid line represents the mean; gray ribbon displays confidence interval. Number of cells: 292 from 6 CARhoA AtL Ecto (red), 162 from 4 CAMypt LtL Ecto (light blue), 325 from 4 DNCdh1 LtL Ecto (lilac), 327 from 9 AtL Ecto (yellow), 327 from 9 LtL Ecto (blue). Statistical test on the final y displacement, Mann-Whitney test: ns, not significant; *$p < 0.05$, **$p < 0.01$, ****$p < 0.0001$. See also Figure S4.

(legend continued on next page)

cohesion and viscosity,[26] and we decreased cell contractility in lateral ectoderm by overexpressing CA myosin phosphatase target subunit 1 (Mypt)[30] prior to performing our transplantation experiments (Figures 6A and 6B; Video S10). Remarkably, the animal ectoderm overexpressing CARhoA transplanted into the lateral ectoderm lost its ability to block animal LME migration. Conversely, LME cells encountering a less-contractile lateral ectoderm overexpressing CAMypt were hindered in their animal-pole-directed migration (Figures 6D–6F, S4G, and S4H). Finally, to directly assess the role of lateral ectoderm cell cohesion for LME migration, we lowered ectodermal cell-cell contact strength by interfering with the function of the cell-cell adhesion receptor cadherin 1 (Cdh1), previously shown to be essential for ectodermal cell-cell contact formation.[31] To this end, we expressed a dominant negative (DN) version of Cdh1 (DNCdh1)[32] in donor embryos and then transplanted DNCdh1-expressing lateral ectoderm into the lateral ectoderm of host embryos (Figure 6C and Video S10). We found that LME migration was strongly inhibited by the less-cohesive DNCdh1-expressing lateral ectoderm (Figures 6D–6F, S4G, and S4H), further supporting the notion that the differences in ectoderm cohesion along the AnVeg axis are responsible for the different activities of animal and lateral ectoderm in modulating LME animal migration.

Depleting BMP affects the non-permissiveness of the animal ectoderm to LME migration

To uncover the molecular pathway patterning tissue cohesion and viscosity within the ectoderm, we analyzed how gene expression differs between lateral and animal ectoderm during LME migration. To this end, we obtained pure populations of either animal or lateral ectoderm cells by expressing a photoactivatable version of the fluorescent protein mCherry1 in wild-type (WT) *tg*(*sebox*::*eGFP*) embryos and then selectively activating it in either the animal or the lateral ectoderm between 6 hpf and 7.5 hpf using a confocal microscope. After photoactivation, we isolated mCherry1-positive cells using fluorescence-activated cell sorting (FACS) and analyzed them by bulk RNA sequencing (RNA-seq) (Figures S5A and S5B). Comparing the expression profiles between animal and lateral ectoderm showed that 54 and 81 genes were differentially expressed in the animal and lateral ectoderm, respectively (adjusted p value < 0.05) (Figure S5B and Table S1). When assigning biological function to those genes, we found that lateral ectoderm preferentially expressed 24 genes encoding for components of six major signaling pathways (29.6% of the total differentially expressed genes [DEGs]). In comparison, the animal ectoderm preferentially expressed five genes encoding for components of only two major signaling pathways (9.25% of the DEGs) (Figure S5B and Table S1). This is consistent with previous observations that the signaling landscapes in the early gastrula differ between the blastoderm margin and animal pole.[33,34] One of the signaling pathways, components of which are differentially expressed between the animal and lateral ectoderm, is BMP signaling, known to be active in both animal and lateral ectoderm.[33–37] Previous studies have shown that BMP signaling is required for LME convergence movements.[17,19] Thus, we asked whether BMP signaling is also important for the onset of the tumbling phase (Figure 1A). To this end, we determined how depletion of BMP signaling affects LME migration. Interestingly, we observed that in *bmp2b* morphant embryos, mesendoderm in both lateral and ventral regions of the gastrula failed to transit into their tumbling phase and, instead, continued migrating toward the animal pole until they collided with the prechordal plate (Figure S5C and Video S11; note that mesendoderm in lateral and ventral regions of *bmp2b* morphants still migrated as loosely associated cells characteristic of their migration in WT embryos, despite these embryos being strongly dorsalized). To assess how BMP signaling specifically within the animal pole affects LME migration, we also performed ectoderm tissue transplantation experiments, replacing the lateral ectoderm of WT embryos with the animal ectoderm of *bmp2b* morphant (*bmp2b* MO) embryos or embryos overexpressing the BMP antagonist *Chordin* (*Chrd*)[38] (Figures 7A and 7B; Video S12). We found that the transplanted BMP-depleted animal ectoderm failed to slow down LME animal migration to a similar extent as transplanted control animal ectoderm (Figures 7C–7I, S5D, and S5E), indicating that BMP signaling is required for the activity of animal ectoderm in slowing down LME animal migration.

Next, we asked whether BMP signaling functions in this process by lowering animal ectoderm tissue cohesion. To this end, we quantified the cell fraction in *bmp2b* MO AtL Ecto transplants and found that it was increased to a level typically found for LtL Ecto transplants (Figure 7F). To test for the specificity of these *bmp2b* knockdown experiments, we injected *bmp2b* MO embryos with mRNA encoding a CA version of the BMP receptor *Alk8* (*CAAlk8*).[39] We found that co-injection of *bmp2b* MO with *CAAlk8* mRNA rescued the *bmp2b* MO ectoderm cell cohesion phenotype (Figure 7F), supporting the specificity of the morphant phenotype.

Finally, to test whether differences in the endogenous activity of BMPs along the dorsal-ventral embryo axis would be sufficient for modulating LME animal migration, we transplanted ventral ectoderm (VtL Ecto), expressing high levels of BMP,[33–35] or dorsal ectoderm (DtL Ecto), expressing lower levels of BMP,[33–35] to the lateral side of host embryos and analyzed the cohesion of the transplanted tissues and their effect on LME animal migration (Figures S6A and S6B; Video S13). We found that the DtL Ecto transplants showed similarly high cohesive (cell fraction) properties as LtL Ecto transplants (Figure S6D), consistent with the notion of low BMP-signaling levels promoting ectoderm cell cohesion. At the same time, however, DtL Ecto transplants turned out to be less permissive to LME migration than LtL Ecto (Figures S6A, S6C, and S6E–S6H), pointing to the

(F) Percentage of most animally migrating LME cells (for definition see Figure S3) in transplanted embryos. Red line represents the median. Number of embryos: 6 CARhoA AtL Ecto (red), 4 CAMypt LtL Ecto (light blue), 4 DNCdh1 LtL Ecto (lilac), 9 AtL Ecto (yellow), 9 LtL Ecto (blue). Statistical test, Mann-Whitney test: ns, not significant; $^{*}p < 0.05$, $^{**}p < 0.01$, $^{***}p < 0.001$. See also Figure S4.
In (E) and (F), datasets for AtL Ecto and LtL Ecto correspond to data shown in Figure 3.

CellPress
OPEN ACCESS

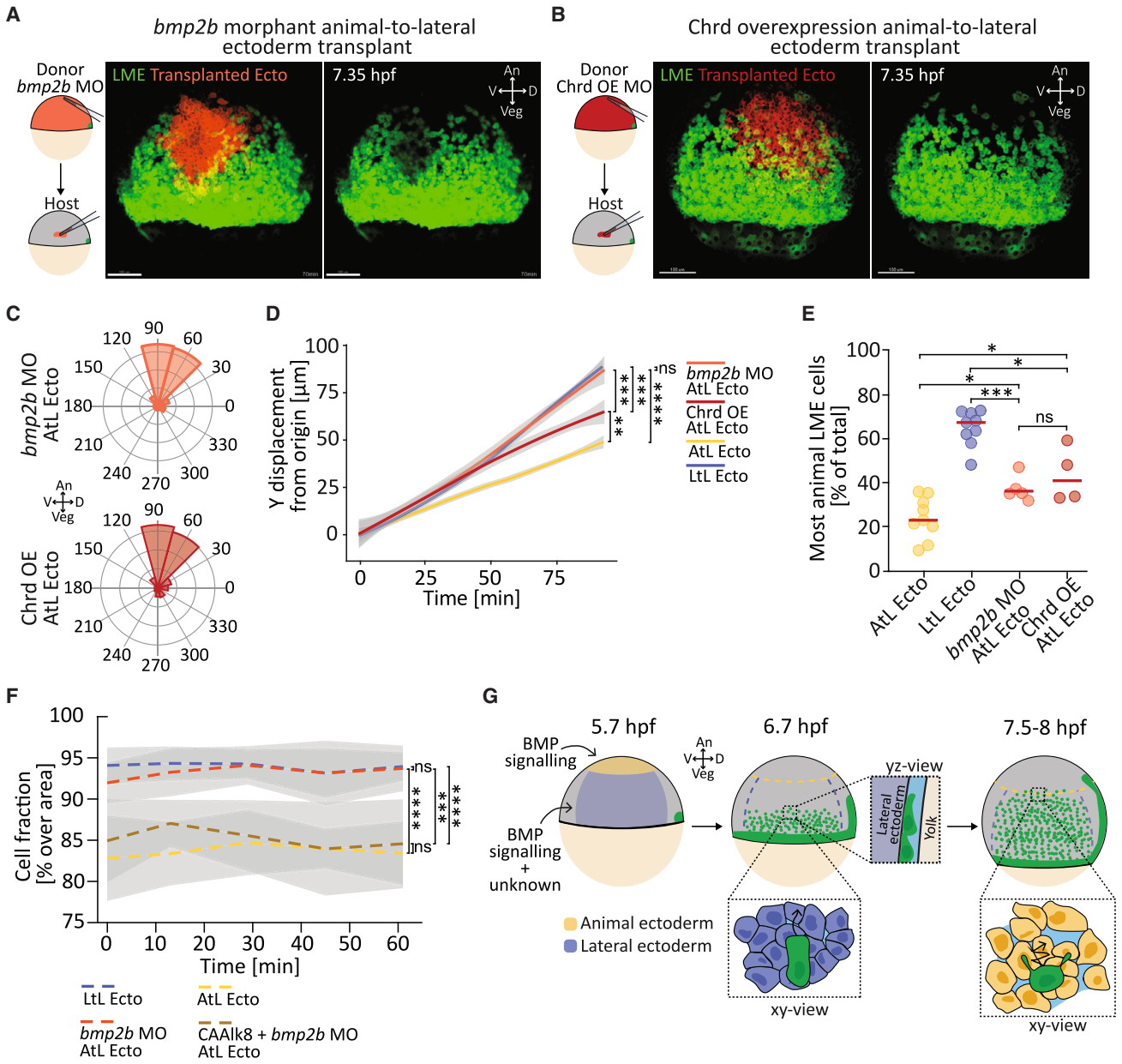

Figure 7. BMP signaling is needed for animal ectoderm blocking animal-pole-directed lateral mesendoderm migration

(A) *bmp2b* morphant (MO) animal-to-lateral (AtL) ectoderm transplant assay. On the left, schematic representation of the experimental setup. On the right, fluorescence images of lateral mesendoderm (LME) cells and transplanted *bmp2b* MO animal ectoderm (*bmp2b* MO AtL Ecto, orange, lateral view) from a representative time-lapse video ~70 min after the start of LME migration (~7.35 hpf). Green, eGFP (LME cells); orange, membrane RFP (*bmp2b* MO AtL Ecto). 2 min 14 s frame rate, t_0 ~6.2 hpf. Scale bar, 100 µm. An, animal; Veg, vegetal; D, dorsal; V, ventral. See also Figure S5 and Video S12.

(B) Chordin-overexpressing (Chrd OE) AtL ectoderm transplantation assay. On the left, schematic representation of the experimental setup. On the right, fluorescence images of LME cells and Chrd OE animal ectoderm (Chrd OE AtL Ecto, cardinal red, lateral view) from representative time-lapse movies ~70 min after the start of LME migration (~7.35 hpf). Green, eGFP (LME cells); cardinal red, 10,000 MW Alexa Fluor 647 dextran (Chrd OE AtL Ecto). ~2 min 12 s frame rate, t_0 ~6.2 hpf. Scale bar, 100 µm. See also Figure S5 and Video S12.

(C) Migration directionality of LME cells in *bmp2b* MO AtL Ecto (orange) and Chrd OE AtL Ecto (cardinal red) embryos. Number of cells, 199 from 5 *bmp2b* MO AtL Ecto (orange), 240 from 4 Chrd OE AtL Ecto (cardinal red).

(D) Displacement (y displacement) along the animal-vegetal (AnVeg) axis of LME cells over time in transplanted embryos. Solid line represents the mean; gray ribbon displays confidence interval. Number of cells: 199 from 5 *bmp2b* MO AtL Ecto (orange), 240 from 4 Chrd OE AtL Ecto (cardinal red), 327 from 9 animal-to-lateral ectoderm transplants (AtL Ecto, yellow), 327 from 9 AtL Ecto (yellow), 327 from 9 LtL Ecto (blue). Dataset for AtL Ecto and LtL Ecto corresponds to data shown in Figure 3. Statistical test on the final y displacement, Mann-Whitney test: ns, not significant; $^{**}p < 0.01$, $^{***}p < 0.001$, $^{****}p < 0.0001$. See also Figure S5.

(legend continued on next page)

possibility that factors, other than BMP-controlled cell cohesion, specific for dorsal ectoderm limit its permissiveness for LME migration. VtL Ecto transplants, in contrast, turned out to be more similar to AtL Ecto transplants in respect of both its cell cohesion and permissiveness for LME migration (Figures S6B–S6H), further supporting a critical role of high BMP signaling lowering ectoderm cell cohesion and thus its permissiveness for LME migration. Collectively, these data indicate that BMP signaling reduces cell cohesion and, thus, tissue viscosity in the animal ectoderm and suggest that the effect of BMP on tissue cohesion is a critical factor rendering this tissue non-permissive for LME animal migration.

The requirement of BMP signaling within the animal ectoderm for halting animal LME migration might be due to BMP-signaling levels differing between the animal and lateral ectoderm or the effect of BMP signaling being differentially modulated by other signaling pathways active in these regions. To distinguish between these possibilities, we analyzed BMP-signaling activity in animal versus lateral ectoderm and found indistinguishable levels of BMP signaling between these regions, as evidenced by an equal nuclear accumulation of phosphorylated Smad1/5, a downstream transcriptional effector for BMP signaling[19] (Figures S6I and S6J). This is consistent with previously published transcriptome datasets[37] showing that both animal and lateral ectoderm express genes (Table S1), the transcription of which has been shown to be directly regulated by BMP signaling.[37] Collectively, these findings suggest that differential modulation of the effect of BMP signaling in the animal versus lateral ectoderm is responsible for the differential capacities of these tissues in facilitating animal LME migration.

DISCUSSION

Our work shows that in the early zebrafish gastrula, the ectoderm plays a decisive role in LME migration by functioning as a substrate controlling LME cell migration. In gastrulation, mesendoderm cells, upon internalization, typically become more mesenchymal and migratory to move away from their site of internalization and migrate to their final destination.[40] We now show that in zebrafish, internalized mesendoderm cells in lateral regions of the gastrula use the overlying ectoderm as their prime substrate for migration (Figure 7G). This choice of a cellular substrate instead of the ECM is likely due to zebrafish embryos showing distinct ECM accumulations only toward the end of gastrulation,[7,8] reminiscent of the situation in *Drosophila*, where the ECM is not yet present during mesoderm migration, and mesoderm cells move dorsolaterally using the ectoderm as their substrate.[41] How LME cells migrate independently of ECM in zebrafish is not yet entirely clear. Previous *in vitro* and *in vivo* studies have suggested that cells undergo ECM-independent migration using cell-cell adhesion or unspecific friction with surrounding structures.[4,42,43] Cell-cell adhesion has been, for instance, proposed in *Drosophila* to be used by both border cells during oogenesis—as a mechanism for cells to generate traction force for migration[44,45]—and mesoderm cells during gastrulation.[41] It is thus conceivable that LME cells use cell-cell adhesion for migrating on the ectoderm, although the precise role of cell-cell adhesion for traction-force generation by LME cells remains to be explored. Alternatively, LME cells might undergo migration by generating friction with their surrounding environment. Such a migration mode has been proposed to be particularly relevant for cells placed in spatial confinement.[4,42,43] However, our finding that reducing spatial confinement by increasing the space between YC and ectoderm in mannitol-injected embryos had no major effect on LME migration argues against LME cells undergoing friction-mediated migration.

We also show that while the majority of LME cells preferentially use the ectoderm as their substrate for migration, the lateral endoderm cells appear to be equally subdivided between those preferring either the ectoderm or the YC. Interestingly, lateral endoderm cells migrating on the ectoderm exhibit more directed and persistent movements than those using the YC as their substrate for migration. It has previously been shown that Nodal signaling promotes the random motion of endoderm cells through Prex1-dependent activation of Rac1.[46] Given that the YSL is an important source of Nodal ligands before gastrulation,[47–49] it is an intriguing possibility that Nodal signals emanating from the YSL trigger random motion of endoderm cells moving on the YC. Yet it still needs to be investigated how lateral mesoderm and endoderm cells choose their substrate for migration and how such a choice of substrate influences their migration directionality and persistence.

One major function of the ectoderm in zebrafish appears to determine how far LME cells can migrate toward the animal pole before switching to their tumbling phase (Figure 7G). In the absence of confinement, there are three main means by which the substrate can affect cell migration[1]: migrating cells can respond to differences in substrate topology, as demonstrated, e.g., in the zebrafish developing optic cup,[50] to gradients of ECM- or cell-bound components, as found, e.g., for immune-cell haptotaxis,[51,52] or to differences in substrate stiffness, as demonstrated, e.g., for neural crest cell migration in *Xenopus*.[53] Our observations suggest that differences in ectoderm viscosity/stiffness are key for LME cells switching to their tumbling phase when getting closer to the animal pole, where ectoderm viscosity is lower. This suggests that LME cells respond to differences in substrate stiffness. However, they do not seem to follow a stiffness gradient, as they can migrate

(E) Percentage of most animally migrating LME cells (for definition see Figure S3) in transplanted embryos. Red line represents the median. Number of embryos: 5 for *bmp2b* MO AtL Ecto (orange), 4 for Chrd OE AtL Ecto (cardinal red), 9 for AtL Ecto (yellow), 9 for LtL Ecto (blue). Datasets for AtL Ecto and LtL Ecto correspond to data shown in Figure 3. Statistical test, Mann-Whitney test: ns, not significant; *$p < 0.05$, ***$p < 0.001$. See also Figure S5.
(F) Cell fraction in *bmp2b* MO AtL Ecto or *bmp2b* MO co-injected with constitutively active Alk8 AtL ectoderm transplants (CAAlk8 + *bmp2b* MO AtL Ecto). Values are shown as mean (dashed line) with SD (light-gray area). Number of embryos: 6 for *bmp2b* MO AtL Ecto (orange), 12 for CAAlk8 + *bmp2b* MO AtL Ecto (gold), 11 for AtL Ecto (yellow), 12 LtL Ecto (blue). Datasets for AtL Ecto and LtL Ecto correspond to data shown in Figure 5. Statistical test, Mixed-effect analysis: ns, not significant; ****$p < 0.0001$.
(G) Schematic of ectoderm-dependent modulation on animal-pole-directed migration of LME cells.

animally on ectoderm tissue with uniformly high tissue viscosity upon overexpression of CARhoA. Rather, they seem to respond to a stiffness threshold, determining whether LME cells can undergo directed migration or tumble. This is similar to neural crest cells in *Xenopus*, which start migrating when the head mesoderm reaches a specific stiffness.[54] How tissue viscosity/stiffness affects the migration mode of LME is still unclear, but mechanosensation is likely to be involved.[13,14,55] The nature of this mechanism is still unknown, but given that LME cells are likely to use cadherin-mediated cell-cell adhesion to migrate along the ectoderm, mechanosensation of the Cdh1 adhesion complex[56,55] might be involved.

While the central role of tissue material properties in various key developmental processes, such as migration of chick hindgut endoderm,[57] *Drosophila* germband extension,[58] *Tribolium* serosa expansion,[59] zebrafish doming,[26] and body axis elongation,[60] becomes increasingly clear, questions remain as to the molecular and cellular mechanisms regulating these properties. We have previously shown that between sphere and dome stage (4–4.3 hpf), the blastoderm undergoes a transient fluidization at its center but not the margin.[26] We further showed that this lack of tissue fluidization at the margin was due to Wnt/planar cell polarity signaling at the blastoderm margin increasing cell cohesion.[26] Our study points to yet another signaling pathway, BMP signaling, being involved in modulating tissue viscosity (Figure 7G). BMP signaling has previously been shown to control the directionality of LME convergence movements by lowering cadherin-mediated cell-cell adhesion in a concentration-dependent manner.[19] This, together with our finding that cell cohesion is lower in animal compared to lateral ectoderm, suggests that one possible pathway through which BMP reduces tissue viscosity in the animal ectoderm is by lowering cadherin-mediated cell-cell adhesion. Interestingly, whereas BMP forms a gradient along the dorsoventral axis of the gastrula,[33–37] with peak levels at the ventral side,[33–37] ectoderm tissue viscosity differs along the AnVeg axis of the ectoderm (Figure 7G). Why BMP lowers ectoderm tissue cohesion only in the animal but not lateral ectoderm is not yet clear, but it is conceivable that other signaling pathways specifically active within the lateral ectoderm might counteract the activity of BMP signaling in lowering tissue viscosity there. In line with this are recent reports showing that BMP target gene expression can be modulated by the co-activation of other signaling pathways, such as the Nodal and FGF pathways.[61]

Limitations of the study

Our study reveals that BMP signaling in the animal ectoderm renders this tissue non-permissive for animal LME migration by reducing tissue cohesion. Interestingly, BMP signaling is also active in the lateral ectoderm but, unlike in the animal ectoderm, it does not diminish tissue cohesion there. This suggests that additional signaling pathways with distinct activities in the animal versus lateral ectoderm might influence the impact of BMP signaling on ectoderm tissue cohesion and its permissiveness for LME migration, a possibility that needs to be further explored.

Furthermore, while our findings identify ectoderm tissue cohesion as a critical determinant of LME migration, other factors, such as variations in surface proteins, may also play a role in regulating LME migration. A comprehensive analysis of the molecular mechanisms driving LME migration on the ectoderm will be necessary to uncover these additional contributing factors.

RESOURCE AVAILABILITY

Lead contact

Further information and requests for resources and reagents should be directed to Carl-Philipp Heisenberg (heisenberg@ist.ac.at).

Materials availability

Plasmids and fish lines generated in this study will be made available on request.

Data and code availability

- RNA-seq data created for this study have been deposited at the Gene Expression Omnibus with the accession number GEO: GSE251904. This paper analyzes existing, publicly available data, accessible at GEO: GSE163047.
- The codes for the minimal model can be found here: https://github.com/dbrueckner/EctodermDeformation.
- The codes for TraXpert are available here: https://zenodo.org/record/5721237.
- The codes for the protrusion directionality analysis and the directness analysis are available here: https://seafile.ist.ac.at/d/f4cfda195434493191d9/.
- Any additional information required to reanalyze the data reported in this paper is available from the lead contact upon request.

ACKNOWLEDGMENTS

We are grateful to the colleagues who contributed to this work with discussions, technical advice, and feedback on the manuscript: Irene Steccari, David Labrousse Arias and the other members of the Heisenberg lab, Nicole Amberg, Florian Pauler, Nicoletta Petridou, Elena Scarpa, and Edouard Hannezo. We also thank the Imaging and Optics Facility, the Life Science Facility, and the Scientific Computing Unit at ISTA for support. The Next Generation Sequencing Facility at Vienna BioCenter Core Facilities performed the RNA-seq for animal and lateral ectoderm. D.B.B. was supported by the NOMIS Foundation as a NOMIS Fellow and by an EMBO Postdoctoral Fellowship (ALTF 343-2022). S. Tavano was supported by an EMBO Postdoctoral Fellowship (ALTF 1159-2018).

AUTHOR CONTRIBUTIONS

Conceptualization, S. Tavano and C.-P.H.; methodology, S. Tavano and D.B.B.; software, S. Tasciyan and R.H.; formal analysis, S. Tavano and D.B.B.; investigation, S. Tavano, D.B.B., and X.T.; resources, R.K. and X.T.; writing – original draft, S. Tavano and C.-P.H.; writing – review & editing, S. Tavano, D.B.B., S. Tasciyan, X.T., A.S., and C.-P.H.; visualization, S. Tavano; funding acquisition, S. Tavano, D.B.B., and C.-P.H.; project administration, C.-P.H.; supervision, C.-P.H.

DECLARATION OF INTERESTS

The authors declare no competing interests.

STAR★METHODS

Detailed methods are provided in the online version of this paper and include the following:

- KEY RESOURCES TABLE
- EXPERIMENTAL MODEL AND SUBJECT DETAILS
  - Fish
- METHOD DETAILS

- Plasmids
- Transgenic zebrafish line generation
- mRNA, morpholino, Mannitol and dextran injections
- Sample fixation and sectioning
- Yolk peeling assay
- Deep-cell transplantations
- Sample preparation for live imaging
- Immunofluorescence
- Imaging setups for live and fixed imaging
- Photoactivation of PAmCherry1 and FACS
- RNAseq

- QUANTIFICATION AND STATISTICAL ANALYSIS
  - LME displacement, delta displacement and difference in LME displacement
  - Protrusion directionality
  - Single cell tracking
  - Ectoderm thickness
  - Cell fraction
  - Cell-cell contacts
  - Relative cell tension
  - Phosphorylated Smad1/5 quantification
  - Transcriptome data processing and analysis
  - Identification of direct transcriptional targets of BMP signaling in the animal and lateral ectoderm
  - Supplementary theory note

SUPPLEMENTAL INFORMATION

Supplemental information can be found online at https://doi.org/10.1016/j.celrep.2025.115387.

Received: July 21, 2023
Revised: August 24, 2024
Accepted: February 11, 2025

REFERENCES

1. SenGupta, S., Parent, C.A., and Bear, J.E. (2021). The principles of directed cell migration. Nat. Rev. Mol. Cell Biol. *22*, 529–547. https://doi.org/10.1038/s41580-021-00366-6.
2. Shellard, A., and Mayor, R. (2020). All Roads Lead to Directional Cell Migration. Trends Cell Biol. *30*, 852–868. https://doi.org/10.1016/j.tcb.2020.08.002.
3. Charras, G., and Sahai, E. (2014). Physical influences of the extracellular environment on cell migration. Nat. Rev. Mol. Cell Biol. *15*, 813–824. https://doi.org/10.1038/nrm3897.
4. Paluch, E.K., Aspalter, I.M., and Sixt, M. (2016). Focal Adhesion–Independent Cell Migration. Annu. Rev. Cell Dev. Biol. *32*, 469–490. https://doi.org/10.1146/annurev-cellbio-111315-125341.
5. Yamada, K.M., Doyle, A.D., and Lu, J. (2022). Cell–3D matrix interactions: recent advances and opportunities. Trends Cell Biol. *32*, 883–895. https://doi.org/10.1016/j.tcb.2022.03.002.
6. Yamada, K.M., and Sixt, M. (2019). Mechanisms of 3D cell migration. Nat. Rev. Mol. Cell Biol. *20*, 738–752. https://doi.org/10.1038/s41580-019-0172-9.
7. Latimer, A., and Jessen, J.R. (2010). Extracellular matrix assembly and organization during zebrafish gastrulation. Matrix Biol. *29*, 89–96. https://doi.org/10.1016/j.matbio.2009.10.002.
8. Jessen, J.R. (2015). Recent advances in the study of zebrafish extracellular matrix proteins. Dev. Biol. *401*, 110–121. https://doi.org/10.1016/j.ydbio.2014.12.022.
9. Solnica-Krezel, L., and Sepich, D.S. (2012). Gastrulation: Making and Shaping Germ Layers. Annu. Rev. Cell Dev. Biol. *28*, 687–717. https://doi.org/10.1146/annurev-cellbio-092910-154043.
10. Pinheiro, D., and Heisenberg, C.-P. (2020). Zebrafish gastrulation: Putting fate in motion. Curr. Top. Dev. Biol. *136*, 343–375. https://doi.org/10.1016/bs.ctdb.2019.10.009.
11. Stock, J., Kazmar, T., Schlumm, F., Hannezo, E., and Pauli, A. (2022). A self-generated Toddler gradient guides mesodermal cell migration. Sci. Adv. *8*, eadd2488. https://doi.org/10.1126/sciadv.add2488.
12. Pézeron, G., Mourrain, P., Courty, S., Ghislain, J., Becker, T.S., Rosa, F.M., and David, N.B. (2008). Live Analysis of Endodermal Layer Formation Identifies Random Walk as a Novel Gastrulation Movement. Curr. Biol. *18*, 276–281. https://doi.org/10.1016/j.cub.2008.01.028.
13. Nair, S., and Schilling, T.F. (2008). Chemokine Signaling Controls Endodermal Migration During Zebrafish Gastrulation. Science *322*, 89–92. https://doi.org/10.1126/science.1160038.
14. Mizoguchi, T., Verkade, H., Heath, J.K., Kuroiwa, A., and Kikuchi, Y. (2008). Sdf1/Cxcr4 signaling controls the dorsal migration of endodermal cells during zebrafish gastrulation. Development *135*, 2521–2529. https://doi.org/10.1242/dev.020107.
15. Sepich, D.S., Calmelet, C., Kiskowski, M., and Solnica-Krezel, L. (2005). Initiation of convergence and extension movements of lateral mesoderm during zebrafish gastrulation. Dev. Dyn. *234*, 279–292. https://doi.org/10.1002/dvdy.20507.
16. Pauli, A., Norris, M.L., Valen, E., Chew, G.-L., Gagnon, J.A., Zimmerman, S., Mitchell, A., Ma, J., Dubrulle, J., Reyon, D., et al. (2014). Toddler: An Embryonic Signal That Promotes Cell Movement via Apelin Receptors. Science *343*, 1248636. https://doi.org/10.1126/science.1248636.
17. Myers, D.C., Sepich, D.S., and Solnica-Krezel, L. (2002). Bmp Activity Gradient Regulates Convergent Extension during Zebrafish Gastrulation. Dev. Biol. *243*, 81–98. https://doi.org/10.1006/dbio.2001.0523.
18. Heisenberg, C.-P., Tada, M., Rauch, G.-J., Saúde, L., Concha, M.L., Geisler, R., Stemple, D.L., Smith, J.C., and Wilson, S.W. (2000). Silberblick/Wnt11 mediates convergent extension movements during zebrafish gastrulation. Nature *405*, 76–81. https://doi.org/10.1038/35011068.
19. von der Hardt, S., Bakkers, J., Inbal, A., Carvalho, L., Solnica-Krezel, L., Heisenberg, C.-P., and Hammerschmidt, M. (2007). The Bmp Gradient of the Zebrafish Gastrula Guides Migrating Lateral Cells by Regulating Cell-Cell Adhesion. Curr. Biol. *17*, 475–487. https://doi.org/10.1016/j.cub.2007.02.013.
20. Ruprecht, V., Wieser, S., Callan-Jones, A., Smutny, M., Morita, H., Sako, K., Barone, V., Ritsch-Marte, M., Sixt, M., Voituriez, R., and Heisenberg, C.P. (2015). Cortical Contractility Triggers a Stochastic Switch to Fast Amoeboid Cell Motility. Cell *160*, 673–685. https://doi.org/10.1016/j.cell.2015.01.008.
21. Chung, W.-S., and Stainier, D.Y.R. (2008). Intra-Endodermal Interactions Are Required for Pancreatic β Cell Induction. Dev. Cell *14*, 582–593. https://doi.org/10.1016/j.devcel.2008.02.012.
22. Ladoux, B., and Mège, R.-M. (2017). Mechanobiology of collective cell behaviours. Nat. Rev. Mol. Cell Biol. *18*, 743–757. https://doi.org/10.1038/nrm.2017.98.
23. Mitra, S.K., Hanson, D.A., and Schlaepfer, D.D. (2005). Focal adhesion kinase: in command and control of cell motility. Nat. Rev. Mol. Cell Biol. *6*, 56–68. https://doi.org/10.1038/nrm1549.
24. Huljev, K., Shamipour, S., Pinheiro, D., Preusser, F., Steccari, I., Sommer, C.M., Naik, S., and Heisenberg, C.-P. (2023). A hydraulic feedback loop between mesendoderm cell migration and interstitial fluid relocalization promotes embryonic axis formation in zebrafish. Dev. Cell *58*, 582–596.e7. https://doi.org/10.1016/j.devcel.2023.02.016.
25. Barriga, E.H., and Mayor, R. (2019). Adjustable viscoelasticity allows for efficient collective cell migration. Semin. Cell Dev. Biol. *93*, 55–68. https://doi.org/10.1016/j.semcdb.2018.05.027.
26. Petridou, N.I., Grigolon, S., Salbreux, G., Hannezo, E., and Heisenberg, C.-P. (2019). Fluidization-mediated tissue spreading by mitotic cell rounding and non-canonical Wnt signalling. Nat. Cell Biol. *21*, 169–178. https://doi.org/10.1038/s41556-018-0247-4.

27. Bruce, A.E.E., and Heisenberg, C.-P. (2020). Mechanisms of zebrafish epiboly: A current view. Curr. Top. Dev. Biol. *136*, 319–341. https://doi.org/10.1016/bs.ctdb.2019.07.001.

28. Petridou, N.I., Corominas-Murtra, B., Heisenberg, C.-P., and Hannezo, E. (2021). Rigidity percolation uncovers a structural basis for embryonic tissue phase transitions. Cell *184*, 1914–1928.e19. https://doi.org/10.1016/j.cell.2021.02.017.

29. Takesono, A., Moger, J., Farooq, S., Cartwright, E., Dawid, I.B., Wilson, S.W., Kudoh, T., and Kudoh, T. (2012). Solute carrier family 3 member 2 (Slc3a2) controls yolk syncytial layer (YSL) formation by regulating microtubule networks in the zebrafish embryo. Proc. Natl. Acad. Sci. USA *109*, 3371–3376. https://doi.org/10.1073/pnas.1200642109.

30. Jayashankar, V., Nguyen, M.J., Carr, B.W., Zheng, D.C., Rosales, J.B., Rosales, J.B., and Weiser, D.C. (2013). Protein Phosphatase 1 β Paralogs Encode the Zebrafish Myosin Phosphatase Catalytic Subunit. PLoS One *8*, e75766. https://doi.org/10.1371/journal.pone.0075766.

31. Krieg, M., Arboleda-Estudillo, Y., Puech, P.-H., Käfer, J., Graner, F., Müller, D.J., and Heisenberg, C.-P. (2008). Tensile forces govern germ-layer organization in zebrafish. Nat. Cell Biol. *10*, 429–436. https://doi.org/10.1038/ncb1705.

32. Grimaldi, C., Schumacher, I., Boquet-Pujadas, A., Tarbashevich, K., Vos, B.E., Bandemer, J., Schick, J., Aalto, A., Olivo-Marin, J.-C., Betz, T., and Raz, E. (2020). E-cadherin focuses protrusion formation at the front of migrating cells by impeding actin flow. Nat. Commun. *11*, 5397. https://doi.org/10.1038/s41467-020-19114-z.

33. Schier, A.F., and Talbot, W.S. (2005). MOLECULAR GENETICS OF AXIS FORMATION IN ZEBRAFISH. Annu. Rev. Genet. *39*, 561–613. https://doi.org/10.1146/annurev.genet.37.110801.143752.

34. Langdon, Y.G., and Mullins, M.C. (2011). Maternal and Zygotic Control of Zebrafish Dorsoventral Axial Patterning. Annu. Rev. Genet. *45*, 357–377. https://doi.org/10.1146/annurev-genet-110410-132517.

35. Tucker, J.A., Mintzer, K.A., and Mullins, M.C. (2008). The BMP Signaling Gradient Patterns Dorsoventral Tissues in a Temporally Progressive Manner along the Anteroposterior Axis. Dev. Cell *14*, 108–119. https://doi.org/10.1016/j.devcel.2007.11.004.

36. Pomreinke, A.P., Soh, G.H., Rogers, K.W., Bergmann, J.K., Bläßle, A.J., and Müller, P. (2017). Dynamics of BMP signaling and distribution during zebrafish dorsal-ventral patterning. Elife *6*, e25861. https://doi.org/10.7554/elife.25861.

37. Greenfeld, H., Lin, J., and Mullins, M.C. (2021). The BMP signaling gradient is interpreted through concentration thresholds in dorsal–ventral axial patterning. PLoS Biol. *19*, e3001059. https://doi.org/10.1371/journal.pbio.3001059.

38. Hammerschmidt, M., Pelegri, F., Mullins, M.C., Kane, D.A., van Eeden, F.J., Granato, M., Brand, M., Furutani-Seiki, M., Haffter, P., Heisenberg, C.-P., et al. (1996). dino and mercedes, two genes regulating dorsal development in the zebrafish embryo. Development *123*, 95–102. https://doi.org/10.1242/dev.123.1.95.

39. Bauer, H., Lele, Z., Rauch, G.-J., Geisler, R., and Hammerschmidt, M. (2001). The type I serine/threonine kinase receptor Alk8/Lost-a-fin is required for Bmp2b/7 signal transduction during dorsoventral patterning of the zebrafish embryo. Development *128*, 849–858. https://doi.org/10.1242/dev.128.6.849.

40. Keller, R. (2005). Cell migration during gastrulation. Curr. Opin. Cell Biol. *17*, 533–541. https://doi.org/10.1016/j.ceb.2005.08.006.

41. Sun, J., Macabenta, F., Akos, Z., and Stathopoulos, A. (2020). Collective Migrations of Drosophila Embryonic Trunk and Caudal Mesoderm-Derived Muscle Precursor Cells. Genetics *215*, 297–322. https://doi.org/10.1534/genetics.120.303258.

42. Bodor, D.L., Pönisch, W., Endres, R.G., and Paluch, E.K. (2020). Of Cell Shapes and Motion: The Physical Basis of Animal Cell Migration. Dev. Cell *52*, 550–562. https://doi.org/10.1016/j.devcel.2020.02.013.

43. Shellard, A., Hampshire, P.A.E., Stillman, N.R., Dix, C., Thorogate, R., Imbert, A., Charras, G., Alert, R., and Mayor, R. (2023). Frictiotaxis underlies adhesion-independent durotaxis. Preprint at bioRxiv. https://doi.org/10.1101/2023.06.01.543217.

44. Cai, D., Chen, S.-C., Prasad, M., He, L., Wang, X., Choesmel-Cadamuro, V., Sawyer, J.K., Danuser, G., and Montell, D.J. (2014). Mechanical Feedback through E-Cadherin Promotes Direction Sensing during Collective Cell Migration. Cell *157*, 1146–1159. https://doi.org/10.1016/j.cell.2014.03.045.

45. Scarpa, E., and Mayor, R. (2016). Collective cell migration in development. J. Cell Biol. *212*, 143–155. https://doi.org/10.1083/jcb.201508047.

46. Woo, S., Housley, M.P., Weiner, O.D., and Stainier, D.Y.R. (2012). Nodal signaling regulates endodermal cell motility and actin dynamics via Rac1 and Prex1. J. Cell Biol. *198*, 941–952. https://doi.org/10.1083/jcb.201203012.

47. Chen, S., and Kimelman, D. (2000). The role of the yolk syncytial layer in germ layer patterning in zebrafish. Development *127*, 4681–4689. https://doi.org/10.1242/dev.127.21.4681.

48. Erter, C.E., Solnica-Krezel, L., and Wright, C.V. (1998). Zebrafish nodal-related 2Encodes an Early Mesendodermal Inducer Signaling from the Extraembryonic Yolk Syncytial Layer. Dev. Biol. *204*, 361–372. https://doi.org/10.1006/dbio.1998.9097.

49. Feldman, B., Gates, M.A., Egan, E.S., Dougan, S.T., Rennebeck, G., Sirotkin, H.I., Schier, A.F., and Talbot, W.S. (1998). Zebrafish organizer development and germ-layer formation require nodal-related signals. Nature *395*, 181–185. https://doi.org/10.1038/26013.

50. Soans, K.G., Ramos, A.P., Sidhaye, J., Krishna, A., Solomatina, A., Hoffmann, K.B., Schlüßler, R., Guck, J., Sbalzarini, I.F., Modes, C.D., and Norden, C. (2022). Collective cell migration during optic cup formation features changing cell-matrix interactions linked to matrix topology. Curr. Biol. *32*, 4817–4831.e9. https://doi.org/10.1016/j.cub.2022.09.034.

51. Weber, M., Hauschild, R., Schwarz, J., Moussion, C., de Vries, I., Legler, D.F., Luther, S.A., Bollenbach, T., and Sixt, M. (2013). Interstitial Dendritic Cell Guidance by Haptotactic Chemokine Gradients. Science *339*, 328–332. https://doi.org/10.1126/science.1228456.

52. Schwarz, J., Bierbaum, V., Vaahtomeri, K., Hauschild, R., Brown, M., de Vries, I., Leithner, A., Reversat, A., Merrin, J., Tarrant, T., et al. (2017). Dendritic Cells Interpret Haptotactic Chemokine Gradients in a Manner Governed by Signal-to-Noise Ratio and Dependent on GRK6. Curr. Biol. *27*, 1314–1325. https://doi.org/10.1016/j.cub.2017.04.004.

53. Shellard, A., and Mayor, R. (2021). Collective durotaxis along a self-generated stiffness gradient in vivo. Nature *600*, 690–694. https://doi.org/10.1038/s41586-021-04210-x.

54. Barriga, E.H., Franze, K., Charras, G., and Mayor, R. (2018). Tissue stiffening coordinates morphogenesis by triggering collective cell migration in vivo. Nature *554*, 523–527. https://doi.org/10.1038/nature25742.

55. Schwartz, M.A., and DeSimone, D.W. (2008). Cell adhesion receptors in mechanotransduction. Curr. Opin. Cell Biol. *20*, 551–556. https://doi.org/10.1016/j.ceb.2008.05.005.

56. Leckband, D.E., and Rooij, J. de (2014). Cadherin Adhesion and Mechanotransduction. Annu. Rev. Cell Dev. Biol. *30*, 1–25. https://doi.org/10.1146/annurev-cellbio-100913-013212.

57. Nerurkar, N.L., Lee, C., Mahadevan, L., and Tabin, C.J. (2019). Molecular control of macroscopic forces drives formation of the vertebrate hindgut. Nature *565*, 480–484. https://doi.org/10.1038/s41586-018-0865-9.

58. Wang, X., Merkel, M., Sutter, L.B., Erdemci-Tandogan, G., Manning, M.L., and Kasza, K.E. (2020). Anisotropy links cell shapes to tissue flow during convergent extension. Proc. Natl. Acad. Sci. USA *117*, 13541–13551. https://doi.org/10.1073/pnas.1916418117.

59. Jain, A., Ulman, V., Mukherjee, A., Prakash, M., Cuenca, M.B., Pimpale, L.G., Münster, S., Haase, R., Panfilio, K.A., Jug, F., et al. (2020). Regionalized tissue fluidization is required for epithelial gap closure during insect

gastrulation. Nat. Commun. *11*, 5604. https://doi.org/10.1038/s41467-020-19356-x.

60. Mongera, A., Rowghanian, P., Gustafson, H.J., Shelton, E., Kealhofer, D.A., Carn, E.K., Serwane, F., Lucio, A.A., Giammona, J., and Campàs, O. (2018). A fluid-to-solid jamming transition underlies vertebrate body axis elongation. Nature *561*, 401–405. https://doi.org/10.1038/s41586-018-0479-2.
61. Rogers, K.W., ElGamacy, M., Jordan, B.M., and Müller, P. (2020). Optogenetic investigation of BMP target gene expression diversity. Elife *9*, e58641. https://doi.org/10.7554/elife.58641.
62. Krens, S.F.G., Möllmert, S., and Heisenberg, C.-P. (2011). Enveloping cell-layer differentiation at the surface of zebrafish germ-layer tissue explants. Proc. Natl. Acad. Sci. USA *108*, E9–E10. https://doi.org/10.1073/pnas.1010767108.
63. Schauer, A., Pranjic-Ferscha, K., Hauschild, R., and Heisenberg, C.-P. (2023). Robust axis elongation by Nodal-dependent restriction of BMP signaling. Development *151*, dev202316. https://doi.org/10.1101/2023.06.19.545591.
64. Lele, Z., Bakkers, J., and Hammerschmidt, M. (2001). Morpholino phenocopies of the swirl, snailhouse, somitabun, minifin, silberblick, and pipetail mutations. Genesis *30*, 190–194. https://doi.org/10.1002/gene.1063.
65. Arboleda-Estudillo, Y., Krieg, M., Stühmer, J., Licata, N.A., Muller, D.J., and Heisenberg, C.-P. (2010). Movement Directionality in Collective Migration of Germ Layer Progenitors. Curr. Biol. *20*, 161–169. https://doi.org/10.1016/j.cub.2009.11.036.
66. Behrndt, M., Salbreux, G., Campinho, P., Hauschild, R., Oswald, F., Roensch, J., Grill, S.W., and Heisenberg, C.-P. (2012). Forces Driving Epithelial Spreading in Zebrafish Gastrulation. Science *338*, 257–260. https://doi.org/10.1126/science.1224143.
67. Iioka, H., Ueno, N., and Kinoshita, N. (2004). Essential role of MARCKS in cortical actin dynamics during gastrulation movements. J. Cell Biol. *164*, 169–174. https://doi.org/10.1083/jcb.200310027.
68. Keller, P.J., Schmidt, A.D., Wittbrodt, J., and Stelzer, E.H.K. (2008). Reconstruction of Zebrafish Early Embryonic Development by Scanned Light Sheet Microscopy. Science *322*, 1065–1069. https://doi.org/10.1126/science.1162493.
69. Kardash, E., Reichman-Fried, M., Maître, J.-L., Boldajipour, B., Papusheva, E., Messerschmidt, E.-M., Heisenberg, C.-P., and Raz, E. (2010). A role for Rho GTPases and cell–cell adhesion in single-cell motility in vivo. Nat. Cell Biol. *12*, 47–53. https://doi.org/10.1038/ncb2003.
70. Weigert, M., Schmidt, U., Boothe, T., Müller, A., Dibrov, A., Jain, A., Wilhelm, B., Schmidt, D., Broaddus, C., Culley, S., et al. (2018). Content-aware image restoration: pushing the limits of fluorescence microscopy. Nat. Methods *15*, 1090–1097. https://doi.org/10.1038/s41592-018-0216-7.
71. Schindelin, J., Arganda-Carreras, I., Frise, E., Kaynig, V., Longair, M., Pietzsch, T., Preibisch, S., Rueden, C., Saalfeld, S., Schmid, B., et al. (2012). Fiji: an open-source platform for biological-image analysis. Nat. Methods *9*, 676–682. https://doi.org/10.1038/nmeth.2019.
72. Berg, S., Kutra, D., Kroeger, T., Straehle, C.N., Kausler, B.X., Haubold, C., Schiegg, M., Ales, J., Beier, T., Rudy, M., et al. (2019). ilastik: interactive machine learning for (bio)image analysis. Nat. Methods *16*, 1226–1232. https://doi.org/10.1038/s41592-019-0582-9.
73. Sommer, C., Straehle, C., Kothe, U., and Hamprecht, F.A. (2011). ILASTIK: INTERACTIVE LEARNING AND SEGMENTATION TOOLKIT. 2011. IEEE Int. Symp. Biomed. Imaging: Nano Macro *1*, 230–233. https://doi.org/10.1109/isbi.2011.5872394.
74. Kimmel, C.B., Ballard, W.W., Kimmel, S.R., Ullmann, B., and Schilling, T.F. (1995). Stages of embryonic development of the zebrafish. Dev. Dyn. *203*, 253–310. https://doi.org/10.1002/aja.1002030302.
75. Kwan, K.M., Fujimoto, E., Grabher, C., Mangum, B.D., Hardy, M.E., Campbell, D.S., Parant, J.M., Yost, H.J., Kanki, J.P., and Chien, C.B. (2007). The Tol2kit: A multisite gateway-based construction kit for Tol2 transposon transgenesis constructs. Dev. Dyn. *236*, 3088–3099. https://doi.org/10.1002/dvdy.21343.
76. Villefranc, J.A., Amigo, J., and Lawson, N.D. (2007). Gateway compatible vectors for analysis of gene function in the zebrafish. Dev. Dyn. *236*, 3077–3087. https://doi.org/10.1002/dvdy.21354.
77. Westerfield, M. (2007). The Zebrafish Book: A Guide for the Laboratory Use of Zebrafish *Danio* ("*Brachydanio*") *rerio* (University of Oregon Press).
78. Hagemann-Jensen, M., Ziegenhain, C., Chen, P., Ramsköld, D., Hendriks, G.-J., Larsson, A.J.M., Faridani, O.R., and Sandberg, R. (2020). Single-cell RNA counting at allele and isoform resolution using Smart-seq3. Nat. Biotechnol. *38*, 708–714. https://doi.org/10.1038/s41587-020-0497-0.
79. Schmidt, U., Weigert, M., Broaddus, C., and Myers, G. (2018). Cell Detection with Star-Convex Polygons (Springer International Publishing), pp. 265–273.
80. Patro, R., Duggal, G., Love, M.I., Irizarry, R.A., and Kingsford, C. (2017). Salmon provides fast and bias-aware quantification of transcript expression. Nat. Methods *14*, 417–419. https://doi.org/10.1038/nmeth.4197.

STAR★METHODS

KEY RESOURCES TABLE

REAGENT or RESOURCE	SOURCE	IDENTIFIER
Antibodies		
Chicken anti-GFP	Aves Lab	Cat# GFP-1020, RRID: AB_10000240
Rat anti-RFP (it recognizes also mCherry)	Chromotek	Cat# 5f8-100, RRID: AB_2336064
Rabbit anti-fibronectin	Sigma-Aldrich	Cat# F3648, RRID: AB_476976
Rabbit anti-Phospho-FAK (Tyr397)	Thermo Fisher Scientific	Cat# 44-624G, RRID: AB_2533701
Rabbit anti-Phospho-Smad1/5 (Ser463/465) (41D10)	Cell Signaling Technology	Cat# 9516, RRID: AB_491015
Mouse anti-Pan-Cadherin antibody clone CH-19	Sigma-Aldrich	Cat# SAB4200731, RRID: AB_2904558
Goat anti-Chicken IgY (H + L) Secondary Antibody, Alexa Fluor™ 488	Thermo Fisher Scientific	Cat# A-11039, RRID: AB_2534096
Goat anti-Rat IgG (H + L) Cross-Adsorbed Secondary Antibody, Alexa Fluor™ 555	Thermo Fisher Scientific	Cat# A-21434, RRID: AB_2535855
Goat anti-Rabbit IgG (H + L) Cross-Adsorbed Secondary Antibody, Alexa Fluor™ 647	Thermo Fisher Scientific	Cat# A-21244, RRID: AB_2535812
Cy™3 AffiniPure™ F(ab')$_2$ Fragment Donkey Anti-Mouse IgG (H + L)	Jackson ImmunoResearch Labs	Cat# 715-166-151, RRID: AB_2340817
Bacterial and virus strains		
One Shot TOP10 Chemically Competent *E. coli*	Thermo Fisher Scientific	Cat# C404010
NEB® 5-alpha Competent *E. coli*	New England Biolabs	Cat# C2987
Chemicals, peptides, and recombinant proteins		
Dextran, Alexa Fluor™ 647 10.000 MW	Thermo Fisher Scientific	Cat# D22914
Dextran Cascade Blue™ 10.000 MW	Thermo Fisher Scientific	Cat# D1976
D-Mannitol	Sigma-Aldrich	Cat# M4125
Paraformaldehyde 16% Solution (methanol-free)	Agar Scientific	Cat# AGR1026
Tissue-Tek® O.C.T. Compound	Sakura Finetek	Cat# 4583
Sucrose	Sigma-Aldrich	Cat# S9378
DAPI (4′,6-diamidino-2-phenylindole, dihydrochloride)	Invitrogen	Cat# D1306
Critical commercial assays		
RNeasy Plus Micro Kit	QIAGEN	Cat# 74034
Deposited data		
Animal vs. lateral ectoderm differentially-expressed genes	This paper	GSE251904
CHX-treated *bmp7* mutants vs. CHX-treated *bmp7* mutants injected with BMP2/7 protein differentially-expressed genes	Greenfeld et al.[37]	GSE163047
Experimental models: Organisms/strains		
Zebrafish: AB wild-type	MPI-CBG Dresden	N/A
Zebrafish: ABxTL wild-type	MPI-CBG Dresden	N/A
Zebrafish: *tg*(*sebox*::*eGFP*)	Ruprecht et al.[20]	ZDB-FISH-150901-6184
Zebrafish: *tg*(*sebox*::*eGFP*); *tg*(*actb2*::*H2A-mCherry*)	This paper	N/A
Zebrafish: *tg*(*actb2*::*H2A-mCherry*)	Krens et al.[62]	ZDB-FISH-150901-29861
Zebrafish: *tg*(*sox17*::*eGFP*)	Chung et al.[21]	ZDB-FISH-150901-15761
Zebrafish: *tg*(*actb2*::*mKate2-tpm3*)	This paper	N/A

(*Continued on next page*)

Continued		
REAGENT or RESOURCE	SOURCE	IDENTIFIER
Zebrafish: *tg(actb2::H2B-mCherry)*	This paper	N/A
Zebrafish: *tg(actb2::mCherry-CAAX)*	This paper	N/A
Oligonucleotides		
Ctrl morpholino: 5′-CCTCTTACCT CAGTTACAATTTATA–3′	Schauer et al.[63]	N/A
Bmp2b morpholino: 5′-CGCGGAC CACGGCGACCATGATC-3′	Lele et al.[64]	ZDB-MRPHLNO-041217-6
Recombinant DNA		
pCS2-H2A-mCherry	Arboleda-Estudillo et al.[65]	N/A
pCS2-LifeAct-RFP	Behrndt et al.[66]	N/A
pCS2-H2B-mKOk	This paper	N/A
pCS2-membraneRFP	Iioka et al.[67]	N/A
pCS2-CARhoA	Keller et al.[29]	N/A
pCS2-CAMypt	Jayashankar et al.[30]	N/A
pCS2-DNCdh1	This paper as described by Grimaldi et al.[32]	N/A
pCS2-Chrd	This paper	N/A
pCS2-CAAlk8	Bauer et al.[39]	N/A
pDestTol2pA2 (attR4-R2)	This paper	NA
pCS2-PAmCherry1	This paper	N/A
pCS2-H2B-eGFP	Keller et al.[68]	N/A
mKOkappa-2A-mTurquoise2	Addgene	CAT# 98837
pENTR-D-TOPO-PAmCherry1-MCS	Addgene	CAT# 60608
pCS2-zfCdh1-eGFP	Kardash et al.[69]	N/A
pCS2-Chordin-Dendra2	Pomreinke et al.[36]	N/A
Software and algorithms		
Content-aware image restoration (CARE)	CSBDeep[70]	N/A
MATLAB	MATLAB Software	N/A
Fiji (Is Just ImageJ)	FiJi[71]	N/A
Imaris	Bitplane	N/A
Prism	GraphPad Software	N/A
R	The R Foundation	N/A
Ilastik	The ilastik developers[72,73]	N/A
ZEN	Carl Zeiss	N/A
TraXpert by Saren Tasciyan	Sixt Lab https://zenodo.org/record/5721237	N/A
Minimal physical model of the differential thinning of the ectoderm layer	This paper https://github.com/dbrueckner/EctodermDeformation	N/A
Protrusion directionality analysis and directness analysis	This paper https://seafile.ist.ac.at/d/f4cfda195434493191d9/	N/A
Illustrator	Adobe	N/A

EXPERIMENTAL MODEL AND SUBJECT DETAILS

Fish

Zebrafish (*Danio rerio*) were housed in 28°C water (pH 7.5 and conductivity 400mS) with a 14 h on/10 h off light cycle. All zebrafish husbandry and breeding were performed in the zebrafish facility at ISTA under standard conditions according to local regulations, and all procedures were approved by the Ethics Committee of ISTA regulating animal care and usage. Embryos were raised in E3 medium and kept at 25°C–31°C until the start of the experimental procedures (4 hpf - 5.7 hpf). After dechorionation and for all experimental procedures preceding live imaging, embryos were kept in Danieau buffer. Staging of the embryos was done according to Kimmel et al.[74]

METHOD DETAILS

Plasmids

All DNA plasmids were extracted and purified using Monarch Plasmid Miniprep Kit (QIAGEN) or EndoFree Plasmid Maxi kit (QIAGEN) following the manufacturer instructions.

The Gateway technology[75,76] was used to generate *pCS2-H2B-mKOk* as follows: the coding sequences for H2B and mKOk were amplified from *pCS2-H2B-eGFP* and from *mKOkappa-2A-mTurquoise2*, respectively. The PCR products were then recombined with *pDONR221* (Lawson#208) for H2B and with *pDONR P2r-P3* (Lawson#211) for mKOk, and subsequently with *pCSDest2* (Lawson#444).

The *pCS2-PAmCherry1* plasmid was generated starting from linearized *pCSDest2* (Lawson#444). The coding sequence for PAmCherry1 was PCR-amplified from *pENTR-D-TOPO-PAmCherry1-MCS*. The fragments were subsequently ligated using NEBuilder HiFi DNA Assembly Cloning Kit (New England Biolabs) following the manufacturer instructions.

The *pCS2-Chrd* plasmid was generated starting from linearized *pCSDest2* (Lawson#444). The coding sequences for Chrd was PCR-amplified as two separate fragments from *pCS2-Chordin-Dendra* using the following primers to remove the Dendra coding sequence.

Chrd fragment 1

(1) pCS2 to Chrd Fwd 5′-CTTTTTGCAGGATCCCATGCCACCATGATGGAGGG-3’
(2) Chrd to Chrd Rev 5′-CATCATCTCCTCGTCCTCCAGAGGGG-3′

Chrd fragment 2

(1) Chrd to Chrd Fwd 5′-AGGACGAGGAGATGATGCAGGCGGA-3’
(2) Chrd to pCS2 Rev 5′-ACTCACTATAGTTCTAGAGGCGTCAGTGTCTCCAGCTTT-3′

The fragments were subsequently ligated using NEBuilder HiFi DNA Assembly Cloning Kit (New England Biolabs) following the manufacturer instructions.

The *pCS2-DNCdh1* plasmid was generated starting from *pCS2-zfCdh1-GFP* and introducing the point mutation W2A as described by Grimaldi et al.[32] In brief, the coding sequence for *cdh1* was PCR-amplified using the following primers (the point mutation is in bold).

(1) pCS2 zfCdh1 Fwd 5′-TTCTTTTTGCAGGATCCCATGCCACCATGGCCTGCGTGACC-3’
(2) zfCdh1 W2A Rev 5′-GAGGGATGAT**AGC**TCCTCTCTTCACGCGCTTGTTCTTG-3’
(3) zfCdh1 W2A Fwd 5′-TGAAGAGAGGA**GCT**ATCATCCCTCCTATCAGCGTGTC
(4) pCS2 zfCdh1 Rev 5′-CTCACTATAGTTCTAGAGGCTAGTCCTCTCCGCCACCGTACATATC-3′

The two fragments were then combined together with overlap extension PCR. The resulting fragment was then assembled with pCS+ plasmid using Gibson Assembly Cloning Kit (New England Biolabs) following the manufacturer instructions.

The *pDestTol2pA2* (*attR4-R2*) destination vector was generated starting from *pDestTol2pA2* (Chien#394). The attR4-R3 recombination sites of *pDestTol2pA2* were excised using the restriction enzymes XhoI and ClaI. The sequence of the attR4-R2 recombination sites was amplified from an existing vector using the following primers.

(1) attR4-R2 Fwd 5′-AACACAGGCCAGATGGGCCCTCAACTTTGTATAGAAAAGTTGAACG-3’
(2) attR4-R2 Rev 5′-TGTCTGGATCATCATCGATGTAATACGACTCACTATAGTTCTAGAGG-3′,

The fragments were subsequently ligated using Gibson Assembly Cloning Kit (New England Biolabs) following the manufacturer instructions.

Transgenic zebrafish line generation

tg(*actb2*::*mKate2-tpm3*), *tg*(*actb2*::*H2B-mCherry*), and *tg*(*actb2*::*mCherry-CAAX*) transgenic lines ubiquitously expressing mKate2-tagged tpm3, mCherry-tagged H2B and membrane-tagged mCherry, respectively, were generated using the Tol2/Gateway technology.[75,76]

For *tg*(*actb2*::*mKate2-tpm3*), the coding sequence of *tpm3* (NCBI reference sequence: NM_201492.2) was amplified using gene specific primers with additional Gateway recombination arms (5′- GGGGACAGCTTTCTTGTACAAAGTGGCTATGGCC GGATCAAACAGC -3′ and 5′- GGGGACAACTTTGTATAATAAAGTTGCTTAGAAACTATTGAGCTCGCTCAG -3′) from cDNA library of sphere stage wild-type Tübingen embryos. The PCR product was recombined with *pDONR P2r-P3* (Lawson#211) and the resulting entry clone was recombined with *pDestTol2pA2* (Chien#394), *p5E β-actin* promoter (Chien#229), and *pME mKate2* to create *pTol2-β-actin:mKate2-tpm3*. The *pTol2* vector was co-injected with mRNA encoding the transposase (Invitrogen) into 1 cell-stage wild-type TL embryos. Individual positive carriers were selected and out-crossed with wild-type TL fish for stable single-copy genetic integration.

For *tg*(*actb2*::*H2B-mCherry*), the coding sequence of H2B was amplified from *pCS2-H2B-eGFP*. The PCR product was recombined with *pDONR P2r-P3* (Lawson#211) and the resulting entry clone was recombined with *pDestTol2pA2* (Chien#394), *p5E β-actin* promoter (Chien#229), and *p3E mCherry+pA* (Chien#388) to create *pTol2:actb2-H2B-mCherry_polA*. The *pTol2* vector was co-injected with mRNA encoding the transposase (Invitrogen) into 1 cell-stage wild-type AB embryos. Individual positive carriers were selected and out-crossed with wild-type AB fish for stable single-copy genetic integration.

For *tg*(*actb2*::*mCherry-CAAX*), the coding sequence of mCherry and of the CAAX motif from the zebrafish *kras* gene were amplified from *p3E mCherry+pA* (Chien#388) and from a cDNA library of larvae stage wild-type AB embryos, respectively, using the following primers

(1) mCherry Fwd 5′-ggggacaagtttgtacaaaaaagcaggcttaATGGTGAGCAAGGGCGAGGAG-3’
(2) mCherry Rev 5′-CTTCTCCTTGTGTTTCTTGTACAGCTCGTCCATGCCG-3’
(3) CAAX Fwd 5′-GCTGTACAAGAAACACAAGGAGAAGATGAGC-3’
(4) CAAX Rev 5′-GGGGACAAGTTTGTACAAAAAAGCAGGCTTAATGGTGAGCAAGGGCGAGGAG-3′

The two fragments were then combined together with overlap extension PCR. The PCR product was recombined with *pDONR 221* (Lawson#208) and the resulting entry clone was recombined with *pDestTol2pA2* (*attR4-R2*) and *p5E β-actin* promoter (Chien#229) to create *pTol2-actb2*::*mCherry-CAAX*. The *pTol2* vector was co-injected with mRNA encoding the transposase (Invitrogen) into 1 cell-stage wild-type AB embryos. Individual positive carriers were selected and out-crossed with wild-type AB fish for stable single-copy genetic integration.

tg(*sebox*::*eGFP*); *tg*(*actb2*::*H2A-mCherry*) transgenic line was generate by crossing the pre-existing *tg*(*sebox*::*eGFP*) and *tg*(*actb2*::*H2A-mCherry*) transgenic lines.

mRNA, morpholino, Mannitol and dextran injections

mRNA transcription was performed using the SP6 mMessage mMachine Kit (Thermo Scientific). Glass capillaries (30-0020, Harvard Apparatus) were pulled using a needle puller (P-97, Sutter Instruments) and mounted on a microinjection system (PV820, World Precision Instruments). Injections at 1-cell and 64-128-cell stages were performed as described.[77] The following mRNAs were injected: 35–50 pg *H2A-mCherry*, 10–15 pg *H2B-mKOk*, 100 pg *membrane-RFP*, 1–2 pg *CARhoA*, 75 pg *CAMypt*, 75 pg *DNCdh1*, 30–40 pg *Chrd*, 30 pg *CAAlk8* and 125 pg *PAmCherry*. For labeling F-actin, 7.5 pg *LifeactRF*P was injected into a single blastomere at 64-128-cell stage. For gene knock-down experiments, the following morpholinos were used in this study: 1.5 ng *bmp2b* MO (5′-CGCGGAC CACGGCGACCATGATC-3′), 1.5 ng Ctrl MO (*human β-globin* MO 5′-CCTCTTACCTCAGTTACAATTTATA–3′). For Mannitol injection, 1 nL of 350 mM Mannitol with 1.25 μg/μL 10.000 MW Alexa Fluor 647 dextran was injected in the interstitial space of sphere/dome stage (4–4.3 hpf) embryos. For labeling the cytoplasm, 1 nL of either 1 μg/μL 10.000 MW Alexa Fluor 647 dextran was injected at 1-cell stage. For labeling the interstitial fluid of embryos, 1 nL of either 1 μg/μL 10.000 MW Alexa Fluor 647 dextran or 1.5 μg/μL 10.000 MW Cascade Blue dextran was injected in the interstitial space of sphere/dome stage (4–4.3 hpf) embryos. To mark the interstitial fluid of embryos after tissue transplantation, 1 nL of 0.5 μg/μL 10.000 MW Alexa Fluor 647 dextran was injected in the interstitial space of late germ ring stage (5.8-5.9 hpf) embryos.

Sample fixation and sectioning

Samples were fixed in 4% paraformaldehyde (PFA) in 1xPBS either for 2 h at room temperature or overnight at 4°C on a shaker. For cryosections, fixed *tg*(*sebox*::*eGFP*) embryos were incubated overnight in 30% sucrose in 1xPBS at 4°C and then embedded in increasing concentrations of OCT medium (0%–15%–30%–50%–75%–90% diluted in 30% sucrose/PBS) at 4°C. Embedded samples were then sectioned to obtain 16 μm cryosections.

Yolk peeling assay

The yolk cell membrane was manually peeled from the blastoderm of *tg*(*sebox*::*eGFP*) or *tg*(*sebox*::*eGFP*); *tg*(*actb2*::*mCherry-CAAX*) embryos at 65–70% epiboly (7–7.5 hpf) using forceps, and both embryo and yolk cell membrane were immediately fixed in 4% paraformaldehyde (PFA). Both blastoderm and yolk cell membrane were then stained with DAPI (nuclei) before imaging.

Deep-cell transplantations

At germ ring stage (5.7 hpf), both host and donor embryos were transferred to Danieau buffer and prepared for transplantation. Using a spike fire-polished transplantation needle with a 20 μm inner diameter (Biomedical Instruments) attached to a syringe system via silicone tubing, ectoderm cells were taken from the donor embryos and placed into the lateral ectoderm of the host embryo (injected with 10–15 pg *H2B-mKO2k* mRNA).

(1) For animal-to-lateral and lateral-to-lateral transplantations, 100–250 cells were transplanted from wild-type *tg*(*sebox*::*eGFP*) donor embryo injected with 10–15 pg *H2B-mKO2k* and 100 pg *membrane RFP* mRNAs to mark nuclei and plasma membrane.
(2) For all others transplantation 200–350 cells were transplanted were transplanted from wildtype *tg*(*sebox*::*eGFP*) donor embryo injected with 10–15 pg *H2B-mKO2k* and 100 pg *membrane RFP* mRNAs to mark nuclei and plasma membrane or 10–15 pg

H2B-mKO2k and 1 ng 10.000 MW Alexa Fluor 647 dextran to mark nuclei and cytoplasm in DNCdh1 LtL transpants, together with either 1–2 pg *CARhoA* mRNA, 75 pg *CAMypt* mRNA, 75 pg *DNCdh1* mRNA, 1.5 ng *bmp2b* MO, 1.5 ng *bmp2b* MO + 30 pg *CAAlk8*, or 40 pg *Chrd* mRNA.

For live imaging, transplanted host embryos were then mounted for upright and inverted imaging, depending on the experimental assay.

For animal-to-animal and lateral-to-animal transplantations, 500–600 cells were transplanted from wild-type *tg*(*sebox*::*eGFP*) donor embryo injected with either 30 pg *H2B-mCherry* and 100 pg *membrane RFP* mRNAs (animal-to-animal ectoderm transplant) or 100 pg *membrane RFP* mRNAs (lateral-to-animal ectoderm transplant) to mark nuclei and plasma membrane, respectively. For fixed imaging, transplanted host embryos were kept in Danieau buffer at 28°C–31°C until fixation.

Sample preparation for live imaging

Embryos were dechorionated and mounted either in 0.65% low melting point (LMP) agarose and put into prepared agarose molds (2%) for up-right imaging or in 0.5% LMP agarose (Invitrogen) on glassbottom dishes (MatTek) for inverted imaging. For all live imaging, the temperature during image acquisition was set to 28.5°C.

Immunofluorescence

Whole mount immunofluorescence, fixed *tg*(*sebox*::*eGFP*); *tg*(*actb2*::*mCherry-CAAX*) embryos were washed in 1xPBS several times before being dechorionated with forceps. Dechorionated embryos were permeabilized in PBSTT (0.1% Triton X-100, 0.1% Tween 20 in PBS) for 30–40 min and then incubated in blocking solution (10% goat serum, 1% DMSO, 0.1% Triton X-100, 0.1% Tween 20 in PBS) for up to 2 h. Embryos were afterward incubated with the primary antibodies diluted in blocking solution for a minimum of one night to a maximum of three days at 4°C. The incubation with fluorophore-conjugated secondary antibodies (diluted 1:500) and DAPI was carried out for 1–2 h at room temperature (RT). Immunofluorescence of cryosections was performed as above with minor changes. Frozen sections were brought to RT and washed three times with 1xPBS, followed by 30 min – 1 h of permineralization with PBSTT, quenched with 0.1 M glycine in PBS for 30 min and incubated with blocking solution for 30 min at room temperature. Embryos were afterward incubated with the primary antibodies diluted in blocking solution overnight at 4°C. The incubation with fluorophore-conjugated secondary antibodies (diluted 1:500) and DAPI was carried out for an 1 h at room temperature. Primary antibody diluition: chicken anti-GFP, 1:1000; rat anti-RFP, 1:500; rabbit anti-fibronectin, 1:200; rabbit anti-Phospho-FAK (Tyr397), 1:200; rabbit anti-Phospho-Smad1/5 (Ser463/465) (41D10), 1:100; mouse anti-Pan-Cadherin antibody clone CH-19, 1:250.

Imaging setups for live and fixed imaging

Upright imaging was performed using either a Zeiss 800 confocal microscope equipped with a Plan-Apochromat 20X/1.0 W objective or a Leica SP8 confocal microscope equipped with an HC FUOTAR L 25x/0.95 W objective. For live imaging, Z-stacks of 58–255 μm with a Z step-size of 1.5 μm and a Z-thickness of 2 μm were acquired every 2–9 min. Inverted imaging was performed using either a Zeiss 800 confocal microscope equipped with a Plan-Apochromat 40X/1.2 W objective or a Leica SP8 confocal microscope equipped with an HC PL APO 40x/1.10 W objective. For live imaging, Z-stacks of 40–75 μm with a Z step-size of 1.5 μm and a Z-thickness of 1 μm were acquired every 2–6 min. Lightsheet imaging was performed using a Zeiss Lightsheet Z with dual acquisition and equipped with 10x/0.2foc illumination objectives and either a 20x/1.0: W Plan-Apochromat Corr DIC; nd = 1.33 (WD = 2.4 mm) or a 20x/1.0: Clr Plan-Neofluar Corr nd = 1.45 (WD = 5.6 m) detection objective. For upright imaging of fixed samples, Z-stacks were acquired with a Z step-size of 1.5 μm and a Z-thickness of 2 μm. For lightsheet imaging of fixed samples, Z-stacks were acquired with a Z step-size of 2–3 μm and a lightsheet thickness of 4.16–4.2 μm.

Photoactivation of PAmCherry1 and FACS

To specifically mark animal or lateral ectoderm, *tg*(*sebox*::*eGFP*) embryos injected with *PAmCherry1* mRNA were mounted for upright imaging and a 444 × 220 × 58.5 μm volume was photoactivated using a 405 nm laser either at the animal pole or on the lateral side. The photoactivation process was composed of 10 cycles of 28 s per embryo in a time window of approximately 90 min from 6 to 7.5 hpf. After photoactivation, embryos were transferred in Ca^{2+}-free Ringer solution and dissociated by gently pipetting using a P-1000 pipette to obtain a single-cell suspension. Per replicate, 5000 PAmCherry1+/eGFP- cells were sorted in 150 μL of RTL plus lysis buffer (RNeasy Plus Micro Kit, QIAGEN) with 1% of 2-mercaptoethanol, briefly vortexed, centrifuged in a small tabletop centrifuge and stored at −80°C until RNA extraction.

RNAseq

Cells were subjected to RNA extraction using RNeasy Plus Micro Kit (QIAGEN) according to the manufacturer instructions. Complete cDNA synthesis and library preparation were performed using SMART-Seq v3 protocol[78] with Nextera UDI adapters. Libraries were then quantified by qPCR (KAPA Biosysytems) and subjected to NovaSeq S4 XP 150-bp pair end sequencing on the NovaSeq 6000 platform, providing on average reads per sample of 92963813.5.

QUANTIFICATION AND STATISTICAL ANALYSIS

LME displacement, delta displacement and difference in LME displacement

Time lapse movies of the embryo lateral side were acquired with a time resolution of approximately 6.2 min. Subsequently, a cross-section view of the embryo was created from a 20 μm-wide volume (Video S1, dashed lines) from the middle of the lateral view using "Reslice/" and "Average Z Projection" plugins in Fiji (Is Just ImageJ) (FiJi). The cross-section view was then used to track the distance covered along the embryo curvature by the front edge of the LME every 23 min, starting from the origin of migration (6.2 hpf) for at least 115 min. The delta displacement was computed as difference of each time point from the previous one. To quantify the difference in LME displacement in the double transplanted embryos, the displacement of the LME front from the margin toward the animal pole (Y axis) was quantified at 8 hpf as average of 4 not overlapping 4 μm-thick optical sections displaying both AtA Ecto and LtA Ecto. Statistical analyses and plots were done using Prisms (GraphPad). Details on the statistical test, sample size and data representation can be found in each figure legends.

Protrusion directionality

Mosaic labelling of LME cells was achieved by injection of 7.5 pg *LifeAct-RFP* mRNA into a single blastomere at the 64/128 cells stage (2–2.25 hpf). Protrusion directionality was quantified as being oriented either toward the ectoderm or yolk cell membrane for an average of 50 min of migration (~2 min 14 s frame rate, t_0 ~6.2 hpf). To compute protrusion directionality, the center and radius of the embryo were determined by approximating the surface shape of the embryo as a sphere and then fitting the embryo surface coordinates obtained by using Spots feature in Imaris (Bitplane). For each cell, the coordinates of the tip of each visible actin protrusions and the cell center were then obtained using Spots feature in Imaris (Bitplane). Using these coordinates, the radial distance was computed as the difference between the protrusion tip position relative to the embryo center and the cell center positions. Value above 0 were defined as ectoderm-directed protrusion, while value below 0 as yolk-directed protrusions. Protrusion length was quantified as distance of the protrusion tip from the cell center. The codes for the protrusion directionality analysis are available here: https://seafile.ist.ac.at/d/f4cfda195434493191d9/. Statistical analyses and plots were done using Prisms (GraphPad). Details on the statistical test, sample size and data representation can be found in the figure legends.

Single cell tracking

For tracking of single cells, time lapse movies were acquired with a temporal resolution of approximately 2 min. If necessary, the spatial resolution of the acquired timelapse images was restored to 1024x1024 pixel after acquisition using Content-aware image restoration (CARE). The nuclear signal (H2B-mCherry or H2B-mKok) was segmented using Surfaces and tracks were computed using the Autoregressive Motion algorithms in Imaris 9 (Bitplane). Each track was subsequentially manually checked and corrected if necessary. In case of cell division, the track of one daughter cell was deleted.

For determining the directedness of migration over time for LME and lateral endoderm cells, the mean alignment of the cell movement with respect to a reference axis was computed as the cosine of the angle between the direction of cell motion at a particular time point and the established reference axis (where 1 equals to no deviation). The codes for the directness analysis are available here: https://seafile.ist.ac.at/d/f4cfda195434493191d9/.

For analyzing the time LME cells spent on the ectoderm, the nuclei of each cell ware used as reference. At each time point, LME or lateral endoderm cells were scored as being placed on the ectoderm when the nucleus was in close proximity with the ectoderm layer. Close proximity was defined as being placed at a distance as equal or less than half nuclear diameter with no or little interstitial fluid (10.000 MW Alexa Fluor 647 dextran) detectable between ectoderm and LME or lateral endoderm nuclei. LME cells were scored as either on the ectoderm or on the yolk cell membrane at each timepoint for ~92 min from the onset of animal migration (6.2 hpf).

For determining the correlation between animal displacement and the time LME cells spent on the ectoderm, the total displacement along the Y axis (Y displacement, corresponding to the AnVeg axis) from the origin and the total time spent of the ectoderm were extracted from the tracking data of each cell.

"First rows after ingression" and "First ingressing cells" refer to LME cells or lateral endoderm cells located in the first 2–3 cell rows at the start of the tracking (6.2 hpf). In the case of transplantation experiments, LME cells were selected only if they were located in an area vegetal to the transplanted ectoderm, in an area that was 1–2 cell diameters smaller in width on the X axis (DV axis) on both sides in comparison to the transplant itself (see Figure S4). "All" refers to LME cells or lateral endoderm cells located in a 300 × 200 μm rectangular area with the front end of this area given by the most animally-located cells at the end of the tracking (7.7 hpf). "Most animal" refers to LME cells or lateral endoderm cells located in a 300 × 100 μm rectangular area with the front end of this area given by the most animally-located cells at the end of the tracking (7.7 hpf).

In transplanted embryos, tracked LME cells were scored as "Most-animally migrating cells" if they were within a 100 μm-wide bin on the Y axis (AnVeg axis) set following the final position of the most-animal LME cells that have not encountered the transplanted ectoderm (See Figure S4).

All but directedness analyses were performed by importing cell migration data in TraXpert or Prisms (GraphPad) for subsequent statistical analyses and plots creation. The analyses and plot creation for directedness of migration over time was done using MATLAB. Details on the statistical test, sample size and data representation can be found in the figure legends.

Supplemental explanation regarding cell migration plots.

(1) For the graphs showing the Time LME or endoderm cells spent on the ectoderm, data were plotted as percentage of total migration time or as relative frequency.
(2) The Migration directionality is shown as rose diagram where each concentric circle represents a different frequency range, with 0 at the center and increasing by 10 for each subsequent circle.
(3) The Displacement along the animal-vegetal axis is quantified as cumulative Y-displacement from the origin of migration (Y axis) and displayed as smooth plot.
(4) Smooth plots for Square displacement and Displacement along the animal-vegetal axis were generated with ggplot's geom_smooth function, which uses local polynomial regression fitting.

Ectoderm thickness

Ectoderm thickness as a function of developmental time was determined in *tg*(*sebox*::*eGFP*); *tg*(*actb2*:: *mKate2-tpm3*) embryos injected with 1 nL of 1 μg/μL 10.000 MW Alexa Fluor 647 dextran to mark interstitial fluid and imaged from either the animal pole or the lateral side of the gastrula with a time resolution of approximately 6.2 min. The fluorescent signals of the LME (eGFP), actin cytoskeleton (mKate2-tpm3) and interstitial fluid (Alexa Fluor 647 dextran) were used to create binary mask of the embryo, the LME, and the interstitial fluid. Subsequently, a cross-section view of the embryo was created from a 20 μm-wide volume from the middle of either the lateral view or the animal pole view, the latter spanning from the lateral to lateral, using the "Reslice/" and "Average Z Projection" plugins in Fiji (Is Just ImageJ) (FiJi). The cross-section views were then used to create a binary mask of the embryo, the LME and the interstitial fluid using Ilastik. To quantify the ectoderm thickness from the binary masks, kymographs were created oriented along the inside-out axis of the tissue at 100 μm intervals, starting either from the animal pole or 100–150 μm animal of the embryo equator. For animal and lateral ectoderm thickness, bins were defined as either lateral ectoderm, in case the ectoderm was in contact with the LME at least for one timepoint during the imaging period, or animal ectoderm in case the ectoderm was not in contact with LME during the entire imaging period. Statistical analyses and plots were done using Prisms (GraphPad). Details on the statistical test, sample size and data representation can be found in each figure legends.

Cell fraction

Time lapse movies were acquired from either the embryo animal pole or the lateral side. In the case of non-transplanted embryos, for each time point 2 non-overlapping z-planes were chosen in the middle of the cell layer closest to the yolk cell membrane. For Figure 5 A and B, wild-type *tg*(*sebox*::*eGFP*) embryos injected with 35 pg *H2A-mCherry* mRNA (nuclei) at the 1-cell stage. At sphere/dome stage (4–4.3 hpf), embryos were injected with 1 nL of 1 μg/μL 10.000 MW Alexa Fluor 647 dextran to mark interstitial fluid. In case transplanted embryos (Figures 5F, 5G, and 7F), cells from a donor *tg(sebox::eGFP)* embryo injected with 35 pg *H2A-mCherry* mRNA to mark nuclei were transplanted at germ ring stage (5.7 hpf) into the lateral ectoderm of a stage-matched wildtype *tg(sebox::eGFP)* host embryo. Host embryos were injected with 1 nl of 0.5 μg/μl 10.000 MW Alexa Fluor™ 647 dextran to mark interstitial fluid after transplantation. For the *bmp2b* morphant animal to lateral transplants (*bmp2b* MO AtL Ecto) and *bmp2b* morphant co-injected with constitutive active Alk8 animal to lateral transplants (CAAlk8 + *bmp2b* MO AtL Ecto), donor embryos were also injected with either 1.5 ng *bmp2b* MO or with 1.5 ng *bmp2b* MO and 30 pg *CAAlk8* mRNA. For the quantification, 1 to 4 not overlapping z-planes were chosen in the middle of the transplant. For each z-plane, the fluorescent signal of 10.000 MW Alexa Fluor 647 dextran was used to create binary masks of the interstitial fluid using Ilastik. The binary masks were then used to quantify the percentage of cell fraction over area using Fiji (Is Just ImageJ) (FiJi). Statistical analyses and plots were done using Prisms (GraphPad). Details on the statistical test, sample size and data representation can be found in the figure legends.

Cell-cell contacts

Time lapse movies were acquired from either the embryo animal pole or the lateral side. Wild-type *tg*(*sebox*::*eGFP*); *tg*(*actb2*::*H2B-mCherry*) embryos injected 100 pg *membrane RFP* (cell membrane) mRNA at the 1-cell stage. At sphere/dome stage (4–4.3 hpf), embryos were injected with 1 nL of 1 μg/μL 10.000 MW Alexa Fluor 647 dextran to mark interstitial fluid. The z-stacks containing the layer of ectoderm cells closest to the yolk were then used for the analysis. From each z-plane of the z-stacks, the fluorescent signal of 10.000 MW Alexa Fluor 647 dextran was used to create binary masks of the interstitial fluid using Ilastik. The binary masks were then used to quantify the percentage of cell perimeter not in contact with interstitial fluid using Fiji (Is Just ImageJ) (FiJi). The cell perimeter was defined as the cell membrane (labeled with membrane RFP) in the z-plane having the widest XY cross-section area of the cell nucleus (labeled with H2A-mCherry). Statistical analyses and plots were done using Prisms (GraphPad). Details on the statistical test, sample size and data representation can be found in the figure legends.

Relative cell tension

Time lapse movies were acquired from either the embryo animal pole or the lateral side. The z-stacks containing the layer of ectoderm cells closest to the yolk were then used for the analysis. From each z-plane of the z-stacks, the fluorescent signal of 10.000 MW Alexa

Fluor 647 dextran was used to create binary masks of the interstitial fluid using Ilastik. The binary masks were then used to determine the presence or absence of interstitial fluid. Contact angles θ were quantified between two ectoderm cells at the interphase with interstitial fluid using the angle tool in Fiji (Is Just ImageJ) (FiJi), with at least one of the two cells being in the z-plane with the widest XY cross-section area of the cell nucleus (labeled with H2A-mCherry). The contact angles were then converted in radiant. The relative cell tension α was then computed as

$$\alpha = \cos\left(\frac{\theta}{2}\right)$$

Statistical analyses and plots were done using Prisms (GraphPad). Details on the statistical test, sample size and data representation can be found in the figure legends.

Phosphorylated Smad1/5 quantification

For the quantification of the immunofluorescence signal of phosphorylated Smad1/5 (pSmad1/5), 1 single 2.5 μm thick optical sections was used for each cryosection. The nuclei of each cell were segmented using the plugin Stardist[79] in Fiji (Is Just ImageJ) (FiJi). Lateral mesendoderm (LME), enveloping layer (EVL) and yolk syncytial layer (YSL) nuclei were excluded according to their position, shape (EVL and YSL) and GFP fluorescence (LME). Lateral ectoderm was defined as 15–25 nuclei per side above the LME, separated from the animal ectoderm by 10–15 nuclei (see also Figure S5C). Animal and lateral ectoderm pSmad1/5 intensities were then quantified as ratio to the DAPI intensity. Statistical analyses and plots were done using Prisms (GraphPad). Details on the statistical test, sample size and data representation can be found in the figure legends.

Transcriptome data processing and analysis

Reads of the same sample on different sequencing lanes were subject to quality checks with fastqc (0.11.7), before and after adapter and quality trimming with trimmomatic (version: 0.38; parameters: 2:30:10 LEADING:3 TRAILING:3 SLIDINGWINDOW:4:15 MINLEN:19). The processed reads were aligned and quantified using Salmon (1.1.0)[80] in mapping based mode, with the –seqBias and –gcBias flags set in order to decrease the hexamer priming and GC content biases. For this quantification, an index created from the zebrafish reference genome (GRCz11) was used. The differential expression analysis was performed using the following libraries: DESeq2 (v. 1.30.1), apeglm (v. 1.12.0), tximport (v. 1.18.0), genefilter (v. 1.72.1) and GenomicRanges (v. 1.42.0). The expression of each gene was expressed as a transcript per million (TPM) value. Differential expression was determined without distinguishing between splice variants of the gene under study and using all protein-coding genes as transcriptome reference. Differentially expressed genes were defined using a cut-off of adjusted P-value <0.05. The statistical analysis and the calculation of the numbers of differentially expressed genes in the various sectors of the Volcano plot were calculated in R using the Enhancedvolcano (1.8.0) and biomaRt (2.46.3) libraries.

Identification of direct transcriptional targets of BMP signaling in the animal and lateral ectoderm

The analysis was performed using a pre-existing RNA-seq dataset.[37] Genes differentially expressed in the either animal or lateral ectoderm were defined as putative direct targets of BMP signaling if they were also differentially expressed in the cycloheximide-treated *bmp7* mutants injected with BMP2/7 protein compared to the uninjected control samples (FDR <0.05, as defined by the authors).[37]

Supplementary theory note

As a minimal physical model of the differential thinning of the ectoderm layer, we used a fluid model with patterned viscosity. In previous work, a simple model for tissue fluidization at the onset of doming predicted the relative thickness change of the blastoderm as two tissues with different viscosities.[26] Here, we generalized this approach to the case of a continuously varying patterned viscosity and applied it to ectoderm morphodynamics in the early gastrula, i.e., a different tissue at a different time of development.

We modeled the ectoderm as an incompressible passive fluid that is extended by an active force f_A at the lateral sides, enforcing a constant expansion speed v. We defined a one-dimensional coordinate system in which the initial tissue is spread from $x = -L$ to $x = L$, where $x = 0$ corresponds to the animal pole, and $x = \pm L$ to the lateral sides. Our aim was to predict the thickness profile $h(x)$ based on assuming a spatially patterned viscosity profile $\eta(x)$.

To this end, we divided the fluid into N elements along the x-axis. Based on incompressibility, we assumed that each fluid element i with thickness h_i and length ℓ_i has a conserved area, and thus

$$\frac{1}{h_i}\frac{dh_i}{dt} = -\frac{1}{l_i}\frac{dl_i}{dt} \qquad \text{(Equation 1)}$$

Assuming the constitutive equation for stress

$$\sigma_{xx} = 2\eta\frac{\partial v_x}{\partial x} - P \qquad \text{(Equation 2)}$$

where η is the viscosity and P the pressure, we get

$$\sigma_{xx,i} = 2\eta_i \frac{1}{l_i}\frac{dl_i}{dt} - P_i \quad \text{(Equation 3)}$$

$$\sigma_{zz,i} = -2\eta_i \frac{1}{l_i}\frac{dl_i}{dt} - P_i \quad \text{(Equation 4)}$$

Applying force balance,

$$\partial_x \sigma_{xx,i} = -F \rightarrow h_i \sigma_{xx,i} = f_A \quad \text{(Equation 5)}$$

$$\sigma_{zz,i} = 0 \quad \text{(Equation 6)}$$

where $F = f_A/(h_i \ell_i)$ is the force density. We then considered an active force that adjusts itself such that the extension speed is constant:

$$\sum_i \frac{dl_i}{dt} = 2v \quad \text{(Equation 7)}$$

Putting everything together, we found

$$\frac{dl_i}{dt} = \frac{l_i}{4h_i\eta_i} f_A \quad \text{(Equation 8)}$$

$$\frac{dh_i}{dt} = -\frac{1}{4h_i} f_A \quad \text{(Equation 9)}$$

and

$$f_A = 8v\left[\sum_i \frac{l_i}{h_i\eta_i}\right]^{-1} \quad \text{(Equation 10)}$$

To compare model predictions to experiment, we used parameters corresponding to the experiment, $v \approx 1.5$ μm/min,[66] $L \approx 500$ μm. Finally, as a single free fit parameter, we estimated the ratio of maximal (lateral) viscosity $\eta_{Lat} = \eta(x = \pm L)$ to minimal (animal) viscosity $\eta_{An} = \eta(x = 0)$ to be $\eta_{Lat}/\eta_{An} \approx 5$.